Analysis of Strengthening and Dissipating Mesoscale Convective Systems Propagating off the West African Coast

ABDOU L. DIENG

Laboratoire de Physique de l'Atmosphère et de l'Océan Siméon Fongang, Cheikh Anta Diop University, Dakar, Senegal

LAURENCE EYMARD

Laboratoire d'Océanographie et du Climat: Expérimentations et Approches Numériques, Pierre et Marie Curie University, Paris, France

SAIDOU M. SALL

Laboratoire de Physique de l'Atmosphère et de l'Océan Siméon Fongang, Cheikh Anta Diop University, Dakar, Senegal

ALBAN LAZAR

Laboratoire d'Océanographie et du Climat: Expérimentations et Approches Numériques, Pierre et Marie Curie University, Paris, France

MARION LEDUC-LEBALLEUR

Laboratoire Atmosphères, Milieux, Observations Spatiales, Pierre et Marie Curie University, Paris, France

(Manuscript received 5 December 2013, in final form 13 August 2014)

ABSTRACT

A large number of Atlantic tropical depressions are generated in the eastern basin in relation to the African easterly wave (AEW) and embedded mesoscale convective systems (MCSs) coming from the African continent. In this paper, the structures of strengthening and dissipating MCSs evolving near the West African coast are analyzed, including the role of the ocean surface conditions in their evolution.

Satellite infrared brightness temperature and meteorological radar data over seven summer seasons between 1993 and 2006 are used to subjectively select 20 cases of strengthening and dissipating MCSs in the vicinity of the Senegal coast. With these observed MCSs, a lagged composite analysis is then performed using Interim ECMWF Re-Analysis (ERA-Interim) and Climate Forecast System Reanalysis (CFSR).

It is shown that the strengthening MCS is generally preceded by prior passage of an AEW near the West African coast. This previous wave trough is associated with a convective cyclonic circulation in the low and middle troposphere, which enhances the southwesterly flow and then provides humidity to the strengthening MCS, located in the vicinity of the subsequent AEW trough. This is favored by the contraction of the wavelength associated with the two troughs. The sea surface contributes to the MCS enhancement through surface evaporation flux. But this contribution is found to be less important than advection of humidity from the previous wave trough. These conditions are almost not found in the dissipating MCS cases, which dissipate in a dry environment dominated by a subsident and anticyclonic circulation, with generally no interaction with a previous wave trough.

1. Introduction

Some tropical depressions observed in the tropical Atlantic basin are initiated on the West African coast. They can cause loss of human life and material damages when they occur near the littoral area, as did Tropical

Corresponding author address: Abdou Lahat Dieng, Laboratoire de Physique de l'Atmosphère et de l'Océan Siméon Fongang, Cheikh Anta Diop University, BP 5085 Dakar, Fann, Senegal.
E-mail: aldlod@locean-ipsl.upmc.fr

DOI: 10.1175/MWR-D-13-00388.1

Storm Cindy in August 1999 (Sall and Sauvageot 2005). The development of tropical disturbances into tropical depressions in the Atlantic basin has been studied for decades and the necessary (but not sufficient) conditions favoring this development have been analyzed. These environmental conditions are attributed to the combination of thermodynamic and dynamical factors (Gray 1975, 1979, 1998). Sea surface temperatures (SSTs) greater than 26.5°C are usually considered to be a necessary condition for tropical cyclone development (Gray 1975, 1979, 1998) and higher SSTs can increase the overall activity in the North Atlantic and Caribbean Sea, especially between 10° and 20°N [also called the main development region (MDR); Goldenberg and Shapiro 1996; Shapiro and Goldenberg 1998; Goldenberg et al. 2001; DeMaria et al. 2001]. By using the National Centers for Environmental Prediction (NCEP) analyses and Geostationary Operational Environmental Satellite (GOES) water vapor imagery, DeMaria et al. (2001) showed that, in the tropical Atlantic, the tropical cyclone generation is mainly limited by the vertical instability and midlevel moisture in the early part of the season, and by the vertical shear at the end of season. Tropical cyclone activity in the North Atlantic region is also strongly influenced by the Saharan air layer (SAL). Since the SAL is associated with very low relative humidity and a strong vertical wind shear in the middle troposphere, many authors argue that the SAL can have a significant negative effect on the genesis of tropical cyclones and their intensification (e.g., Dunion and Velden 2004, and others). On the contrary, some studies (e.g., Karyampudi and Carlson 1988; Karyampudi and Pierce 2002; Jenkins and Pratt 2008; Jenkins et al. 2008) suggested a potential positive influence on the growth of easterly waves and tropical cyclones in the Atlantic. The real effect of SAL on tropical cyclone activity is not fully resolved. Based on European Center for Medium-Range Weather Forecasts (ECMWF) analyses, *Meteosat-9* images, and National Hurricane Center best track archives, Arnault and Roux (2011) suggested that the simultaneous presence of intense wave troughs with deep convection and low-level cyclonic circulation between the northeasterly trade winds and the southwesterly monsoon flow is necessary for tropical cyclone genesis in the Cape Verde region (located between the West African coast and 30°W).

However, tropical cyclone genesis cannot occur in an absence of a preexisting disturbance of sufficient amplitude such as an easterly wave, monsoon depression, or even a baroclinic cyclone (McBride and Zehr 1981; Briegel and Frank 1997; Gray 1998). The mesoscale convective systems (MCSs) are characterized by a mesoscale cyclonic vortex (MCV) in the middle layers. Many studies such as Menard and Fritsch (1989), Bister and Emanuel (1997), Ritchie and Holland (1997), and Simpson et al. (1997) suggest that these MCVs could play a role in the tropical cyclogenesis. Bister and Emanuel (1997) suggested that the MCV advection to the lower layers is favored by stratiform precipitation cooling in MCSs. Simpson et al. (1997), as well as Ritchie et al. (2003), hypothesized that this occurs when two or more MCSs interact. According to this idea, each MCS spins up its own MCV in the stratiform region of the MCS; when two or more MCVs are in close proximity, they begin to rotate around a common axis and amalgamate into a common vortex (see Houze 2004).

The weather in West Africa in boreal summer is characterized by the presence of transient synoptic disturbances, called African easterly waves (AEWs), with wavelengths of 2000–4000 km (e.g., Reed et al. 1977; Carlson 1969; Diedhiou et al. 1999). They have been known for decades as the dominant synoptic weather systems in West Africa. They also are major dynamical precursors for growth/decay MCS over West Africa (Fink and Reiner 2003; Kiladis et al. 2006) and most of tropical cyclones in the MDR are initiated from these waves (Pasch et al. 1998; Thorncroft et al. 2007; Hopsch et al. 2007). By comparing developed and nondeveloped AEWs with embedded MCSs off the West African coast, using ECMWF reanalyses and brightness temperatures from the Cloud Archive User Service (CLAUS), Hopsch et al. (2010) showed that developed AEWs are characterized by more pronounced cold core structure two days before their arrival at the coast.

Tropical cyclone genesis off the West African coast can thus result from interactions between AEWs and MCSs. Berry and Thorncroft (2005) studied the impact of the Guinea highlands on strengthening AEWs near West African coasts. They suggest that potential vorticity at 600–700 hPa, associated with AEWs, can merge with potential vorticity generated by the convection that developed on Guinea highlands before arrival of the AEWs. The merger of these two cores favored the genesis of Tropical Depression Alberto off the Guinea coast in August 2000, confirming Simpson et al.'s observations. Chiao and Jenkins (2010) argued in a modeling case study that the passage of the squall line associated with the redevelopment of convection on the Guinea highlands was responsible for the production of potential vorticity in the lower and middle layers of the MCS, which then became Tropical Depression Debby off the Guinea coast in August 2006. They showed that the blocking (i.e., flow deflection) effects from the highlands made an important contribution to the vortex development off the coast of Guinea, confirming Berry and Thorncroft's (2005) hypothesis. Arnault and Roux (2010) investigated the contribution of convective

processes in the generation and maintenance of cyclonic vorticity within developing and nondeveloping AEW trough off the West African coast during their ''continental'' and ''oceanic'' transition stages. They showed that convective process played an important role on the production of low to midlevel cyclonic vorticity through tilting and stretching, in particular in the developing case where it was stronger. Moreover the MCS position within the AEW sector (northerly, southerly, trough, and ridge phase; see Fink and Reiner 2003) is considered as an important factor for tropical cyclone genesis. Deep convection is generally observed in the AEW trough when it develops into a tropical depression (Hopsch et al. 2010; Arnault and Roux 2011; Leppert et al. 2013). Recent studies of Leppert et al. (2013) revealed that the coverage area evolution by convection in the trough and southerly sectors of AEW before genesis could be a key factor in determining whether an AEW will develop into tropical depression off the western African coasts or not. However, a small percentage of AEWs (about 6%) developed close to the coast (east of 30°W; Arnault and Roux 2010; Hopsch et al. 2010), and the actual causes of development or dissipation of MCSs in relation with AEWs during their evolution in this region remain an open question. The nature of such MCSs and the contribution of air–sea flux exchange on MCS evolution have not been widely examined yet.

The objective of this work is to statistically analyze the structures of strengthening and dissipating MCS near the West African coast and to evaluate the role of AEW occurrence and oceanic surface conditions on their evolution. Section 2 presents data used and the methodology. Section 3 describes the mean conditions occurring in western Africa and the adjacent tropical Atlantic during the boreal summer. Section 4 provides composite analysis of some specific characteristics of strengthened and dissipated MCSs in the western African coast. In sections 5 and 6 the role of AEWs on the evolution of MCS cases, and the oceanic surface conditions prevailing before and after passage of the strengthening MCSs are examined. A discussion and conclusions are given in sections 7 and 8.

2. Data and methodology

a. Observational data

The meteorological Dakar radar is located at the Dakar (Senegal) airport (14°34′N, 17°29′W, altitude 30 m). It is dedicated to the operational observations of the Agence Nationale de l'Aviation Civile et de la Météorologie du Sénégal (ANACIM) and of the Agence pour la Sécurité de la Navigation Aérienne (ASECNA). It is activated only during precipitation events. The technical characteristics of this radar were documented by Nzeukou and Sauvageot (2002). Its data provide rain event monitoring in a radius of about 250 km around Dakar with recording periods between 10 and 20 min. This radar was used by Nzeukou and Sauvageot (2002) to describe and discuss the characteristics of the rainfall distribution in Senegal's coastal regions. Data obtained between July and September from 1993 to 1999 are used for the present study.

In addition, the thermal infrared brightness temperatures from the CLAUS dataset (see Hodges et al. 2000) are used to increase the number of case studies and to extend the monitoring of the systems selected using radar data. Data are provided on a regular 0.5° latitude × 0.5° longitude horizontal grid with a 3-h record. These data have been used by Hopsch et al. (2010) to compare convective activities associated with developing and nondeveloping AEWs near the western African coast and the north tropical Atlantic region.

Brightness temperature data of the thermal infrared channel (10.8 μm) from the Spinning Enhanced Visible and Infrared Imager (SEVIRI) instrument on board Meteosat Second Generation (MSG) are widely used to analyze the properties of convective systems (Maddox 1980; Mapes and Houze 1993). Brightness temperature thresholds of 233 and 213 K are most commonly used to identify deep convection and very deep convection over West Africa (Mathon and Laurent 2001). Here, the brightness temperature data from MSG are used to detect MCS in the vicinity of the West African coast. The data have a 15-min temporal and a 3-km spatial resolution. Thanks to the African Monsoon Multidisciplinary Analyses (AMMA; http://database.amma-international.org/). these data were obtained from July to September 2006. Indeed, this season is particularly interesting because the National Aeronautics and Space Administration (NASA) AMMA (NAMMA; Zipser et al. 2009) field campaign, of which one of key objectives was the characterization of tropical cyclogenesis, took place during this season.

b. Reanalyses

Two sets of reanalyses are used to analyze the MCSs structure and their evolution in the vicinity of the western African coast: the latest ECMWF global atmospheric reanalysis [the Interim ECMWF Re-Analysis (ERA-Interim)] and the third reanalysis product [the Climate Forecast System Reanalysis (CFSR)] from the National Centers for Environmental Prediction (NCEP). However, it should be noted that these reanalyses are subject to errors due to the lack of observations in this region and the deficiencies of model parameterizations in tropical areas (Meynadier et al. 2010). Despite this limitation, great efforts were made in terms of spatial resolution during the last decade to make them more realistic with

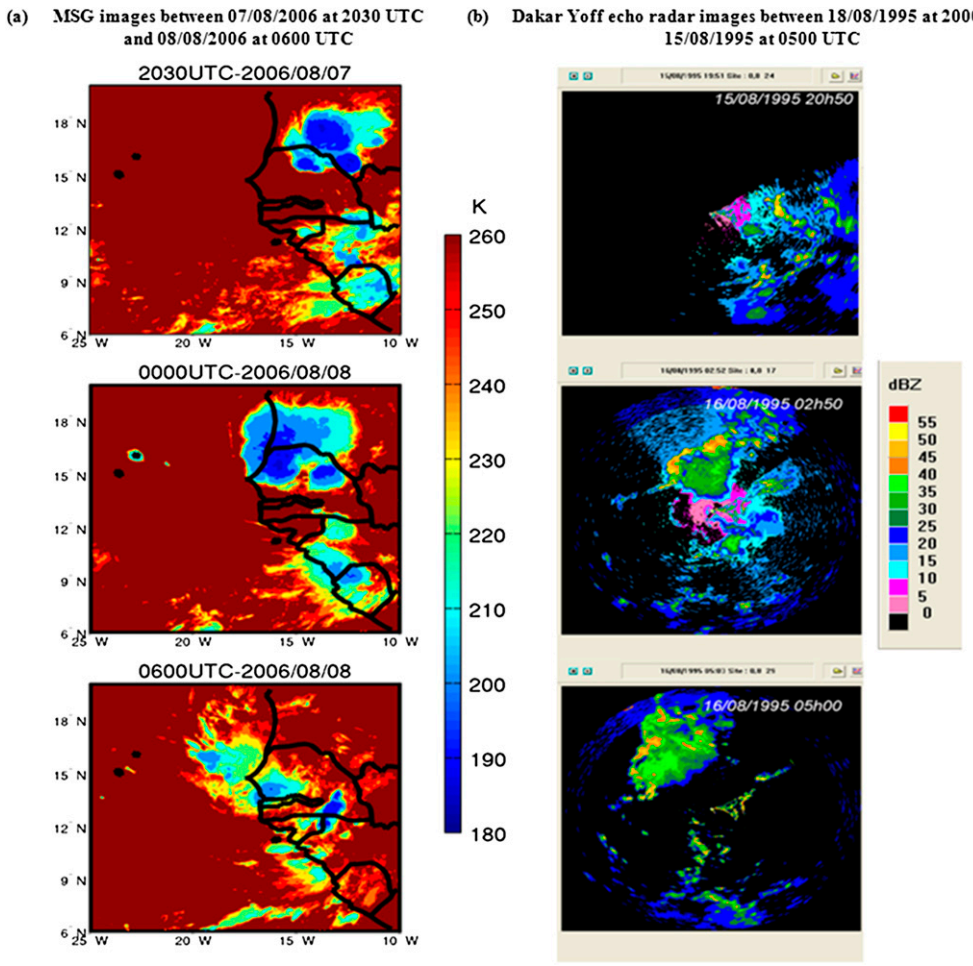

FIG. 1. (a) MSG brightness temperature images of the thermal infrared channel (10.8 μm) showing an MCS that dissipates a few hours after crossing the northwest Senegalese coast about 0000 UTC 8 Aug 2006. (b) Radar images of an MCS that strengthens at the same region about 0500 UTC 16 Aug 1995.

respect to observations. They therefore probably represent the best consistent four-dimensional dataset of the MCSs' atmospheric environment and large-scale atmospheric features. The July–September period between 1993 and 1999 and of the year 2006 are used in this work to fit with observed MCS cases.

The ERA-Interim reanalyzed fields are available on a 0.75° horizontal grid; the vertical atmospheric profiles are retrieved on 27 levels from 1000 to 100 hPa, with 6-hourly data (0000, 0600, 1200, and 1800 UTC). Information about the model description, data assimilation method, and input datasets used to produce ERA-Interim are given in Dee et al. (2011). ERA-Interim fields have been used in several studies in the Sahel region (e.g., Berry and Thorncroft 2005).

CFSR is a global, high-resolution, coupled atmosphere–ocean–land surface–sea ice system designed to provide the best estimate of the state of these coupled domains over a 31-yr period starting in 1979 (Saha et al. 2010). Reanalyzed fields have a 0.5° horizontal resolution and are available every 6 h (0000, 0600, 1200, and 1800 UTC). As in ERA-Interim, the vertical atmospheric profiles are retrieved on 27 levels from 1000 to 100 hPa.

c. *Criteria for MCS case selection*

MSG, radar images, and CLAUS data are used to select MCS cases. MCSs are characterized when they overpass the coast (see Fig. 1). Selection of either strengthening or dissipating MCSs is subjectively made by monitoring their diameter/surface size evolution with time. Selected systems cover an area greater than 10 000 km^2 for more than 18 h and have a brightness temperature below the threshold of 233 K over land. While strengthening MCSs have an increasing size within the next 24 h over ocean (characterized by a low brightness temperature area), dissipating MCS disappear from satellite images a few hours after leaving the coast.

TABLE 1. Selected MCSs near Senegalese coast between 1993 and 2006. Systems that became associated with tropical storms east of 40°W noted by the NHC are also shown in the table.

	Strengthening MCS cases			Dissipating MCS cases	
MCS No.	Crossing date	Observation tool	Associated named tropical storm date and position	Crossing date	Observation tool
1	1750 UTC 31 Jul 1993	Radar		1800 UTC 27 Jul 1993	CLAUS
2	1200 UTC 18 Jul 1993	CLAUS		0000 UTC 9 Aug 1993	CLAUS
3	2300 UTC 10 Aug 1994	Radar	Chris 1200 UTC 16 Aug 1994, 11.3°N, 39.4°W	1310 UTC 9 Aug 1994	Radar
4	1200 UTC 14 Aug 1994	CLAUS		0600 UTC 20 Jul 1995	CLAUS
5	0600 UTC 16 Aug 1995	Radar	Humberto 0000 UTC 22 Aug 1995, 13.2°N, 33.0°W	0000 UTC 8 Sep 1995	CLAUS
6	0600 UTC 22 Aug 1996	CLAUS	Fran 1200 UTC 23 Aug 1996, 14°N, 21°W	0600 UTC 11 Jul 1996	CLAUS
7	2110 UTC 25 Aug 1995	Radar		1800 UTC 18 Jul 1996	CLAUS
8	0550 UTC 30 Aug 1995	Radar		0000 UTC 7 Aug 1996	Radar
9	1800 UTC 17 Aug 1998	CLAUS		0000 UTC 27 Sep 1996	Radar
10	0600 UTC 14 Sep 1998	CLAUS		1630 UTC 26 Aug 1998	Radar
11	0810 UTC 16 Sep 1998	Radar	Ivan 0000 UTC 19 Sep, 13.4°N, 26.6°W	1300 UTC 29 Jul 1999	Radar
12	1200 UTC 21 Aug 1998	CLAUS	Jeanne 0600 UTC 21 Sep 1999, 9.6°N, 17.4°W	0000 UTC 25 Jul 1996	Radar
13	0540 UTC 18 Aug 1999	Radar	Cindy 0000 UTC 19 Aug 1999, 13.5°N, 18.9W	2340 UTC 14 Aug 1999	Radar
14	0240 UTC 29 Aug 1999	Radar		2330 UTC 2 Aug 2006	MSG
15	2300 UTC 16 Jul 2006	MSG		0000 UTC 8 Aug 2006	MSG
16	0230 UTC 21 Jul 2006	MSG		0000 UTC 12 Aug 2006	MSG
17	1800 UTC 26 Jul 2006	MSG		1200 UTC 31 Aug 2006	MSG
18	0600 UTC 14 Aug 2006	MSG		0545 UTC 2 Sep 2006	MSG
19	1800 UTC 20 Aug 2006	MSG	Debby 1800 UTC 21 Aug 2006, 11.6°N, 21.7°W	0445 UTC 18 Sep 2006	MSG
20	1200 UTC 11 Sep 2006	MSG	Helene 1200 UTC 11 Sep 2006, 11.9°N, 22.0°W	0600 UTC 26 Sep 2006	MSG

Figure 1 shows examples of 1) an MCS, detected in MSG images, which begins to dissipate at about 0600 UTC 8 August 2006, northwest of Dakar, Senegal, and 2) another MCS observed with the Dakar Yoff Radar. The latter reintensified between 2000 and 0500 UTC 16 August 1995 and became Tropical Depression Humberto on 22 August 1995 at 13.3°N, 33.0°W (Sall et al. 2006). Note that in these cases the strengthening or dissipation process occurs within 24 h. Consequently, given this short time range, the analysis of MCS properties is made at every time step in the reanalyses (6 h).

Table 1 gives the approximate passage dates of selected MCSs. Strengthening MCS numbers 19 and 20 and dissipating MCS numbers 17, 18, and 20 were studied by Jenkins et al. (2010) during the special observation period 3 (SOP3) phase of the AMMA field campaign in 2006. Most of MCSs selected using radar data were tracked by Sall et al. (2006). Finally, 20 strengthening and 20 dissipating MCSs cases were selected near the western African coast between 11° and 15°N (see Table 1 and Fig. 2). The CLAUS data allowed us, in concert with the ERA-Interim fields, to identify, among the strengthening MCS cases, those which were named systems by the National Hurricane Center (see Table 1) between the coast and the longitude 40°W.

d. *MCS composite building*

The characteristics of the strengthening and dissipating MCS are studied using composites of the selected cases. Two sets of composites are generated using ERA-Interim and CFSR reanalyses: one for the strengthening cases and one for the dissipating cases. The reference date (H00) is taken as the time when a convective system, as observed by radar, MSG, or CLAUS, just crosses the coast. For the reanalyses (ERA-Interim and CFSR), it is the closest analysis time. Composites are computed every 6 h backward and forward four days from H00.

Note that 18°W is denoted the first reanalysis grid longitude west of the coastline and chosen as the reference longitude (hereinafter Xref). However, MCSs do not all cross the coast at the same latitude at H00 (Fig. 2). To properly superimpose the MCS patterns, composites are built by shifting the MCS latitude center to the same virtual latitude, taken as the reference latitude (Yref).

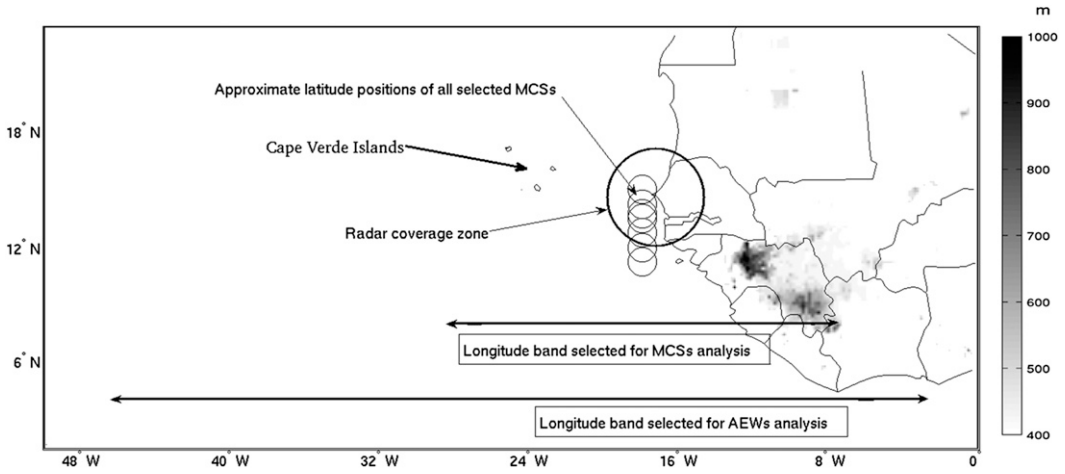

FIG. 2. Map of West Africa with relief over 500 m shaded. The approximate coverage zone of the meteorological Dakar radar is indicated by the black circle. The small circles give the approximate latitude positions of selected MCSs. The shorter (longer) horizontal bar shows the band of longitude selected for MCS (AEW) analysis. The location of the meteorological Dakar radar is indicated by the center of bigger circle.

This virtual latitude corresponds to the mean propagation direction of MCS when it crosses the coastline. The final composite at H00 is thus located at Yref, corresponding to the mean latitude position of the MCS, and at Xref (18°W), the closest reanalysis grid longitude to the coast.

To highlight the composite characteristics, the mean seasonal evolution is removed from reanalyses by subtracting at each time step the corresponding 30-day moving average field. To check the robustness of the composite results, the significance of each data composite is tested using the Monte Carlo method. It consists of 1000 experiments in which 20 random dates in the July–September period between 1993 and 2006 are generated. The 901st value among the sorted 1000 resulting composites gives the 10% significant threshold.

3. Mean conditions over western Africa and the eastern tropical Atlantic during the July–September period

This section briefly describes the large-scale environment for the selected MCSs, using monthly means of July, August, and September for years during which the MCSs were selected. Prevailing weather conditions during the rainy season (monsoon) over western Africa and the eastern tropical Atlantic has been widely documented in earlier studies (e.g., Kiladis et al. 2006; Thorncroft et al. 2011).

Figure 2 shows the latitudes of all selected MCSs as they propagate off the West African coast. The MCS coastal latitude ranges between 9° and 16°N, the mean latitude being around 13°N. This latitude band is included in the main development region, which was defined by Goldenberg and Shapiro (1996) as the principal region of cyclone development in the tropical Atlantic.

a. Mean patterns at 700 hPa

Figure 3 show the mean monthly horizontal fields of relative humidity, wind, and positive relative vorticity at 700 hPa from July to September with ERA-Interim (left) and CFSR (right). The mean circulation at 700 hPa is dominated by the African easterly jet (AEJ) whose maximum wind (12 m s^{-1}) is located between 12° and 18°N. Maxima of relative humidity and positive relative vorticity are located just south of the AEJ. This region, favorable to barotropic conversion, supports traveling AEWs to the south of the AEJ (Pytharoulis and Thorncroft 1999). Over the continent, the relative vorticity maximum is located over the Guinea highlands (around 9°N, 10°W). Between July and September the meridional gradient of relative humidity decreases toward the north of the AEJ as the intertropical convergence zone (ITCZ) migrates northward. The CFSR exhibits a stronger AEJ and greater amount of relative humidity than ERA-Interim for the three months at this pressure level. The relative humidity maximum ranges between 75% and 85% for CFSR for the three months and between 65% and 70% for ERA-Interim.

b. Mean patterns at 850 hPa

Figure 4 presents the same fields as in Fig. 3 but at 850 hPa. Relative humidity is greater at the south due to the northeastward monsoon flow, which carries moist air to the continent. This low-level flow is stopped north of 12°N by the opposite warm and dry winds coming from

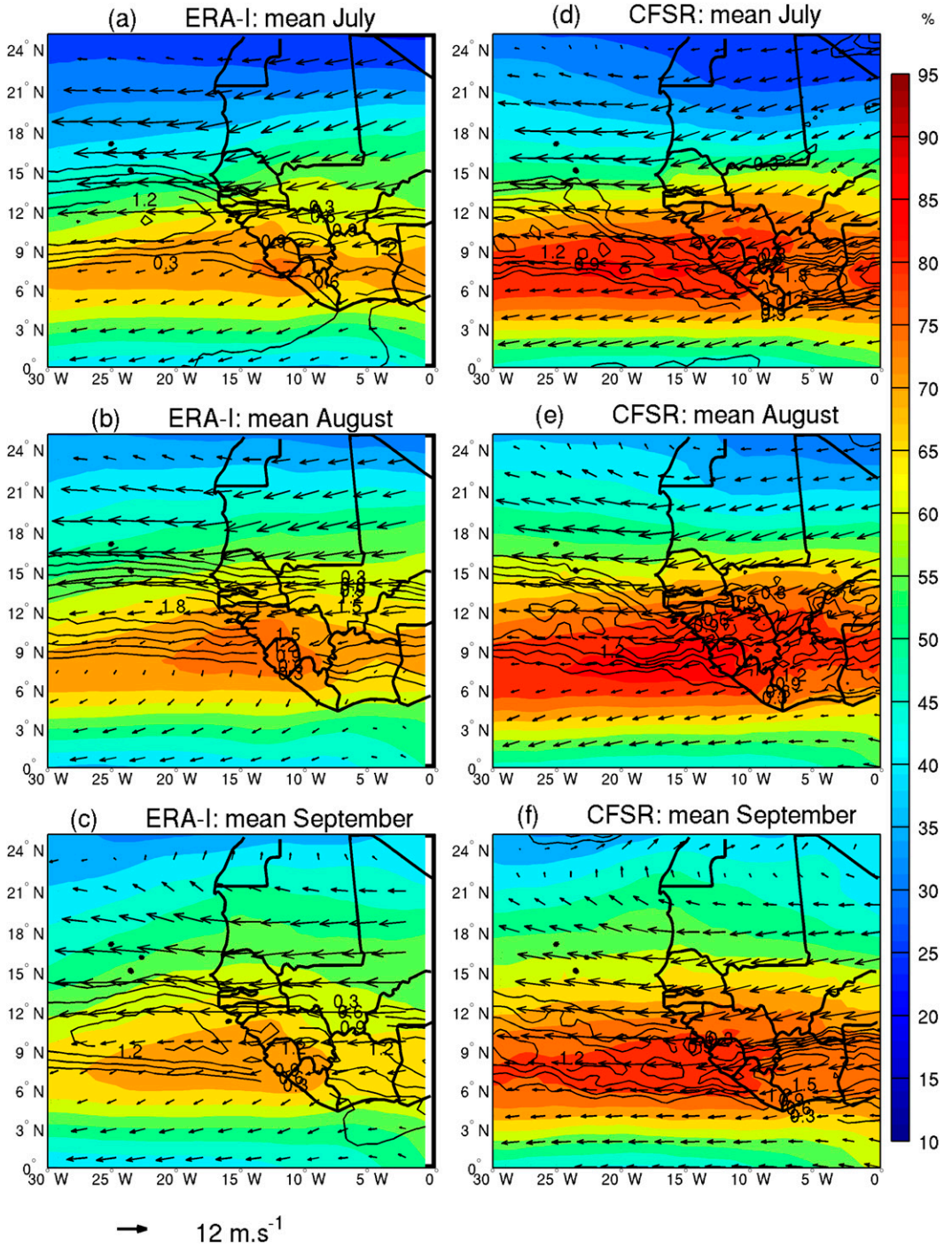

FIG. 3. Mean fields at 700 hPa of relative humidity (colors, %), wind (arrows, $m\,s^{-1}$), and positive relative vertical vorticity (contours, $\times 10^{-5}\,s^{-1}$) of (a),(d) July, (b),(e) August, and (c),(f) September with (left) ERA-Interim and (right) CFSR. The fields were only averaged over the years including the dates of selected MCSs.

the Sahara and the northerly wind from the Canary Islands, both merging into the trade winds. The convergence zone between opposite flows corresponds to the ITCZ over the ocean. Positive relative vorticity is found in two areas on both sides of the AEJ over the continent, corresponding to the mean AEW trough tracks. The north waves propagate in association with dry baroclinic energy conversions at the southern boundary of the Sahara

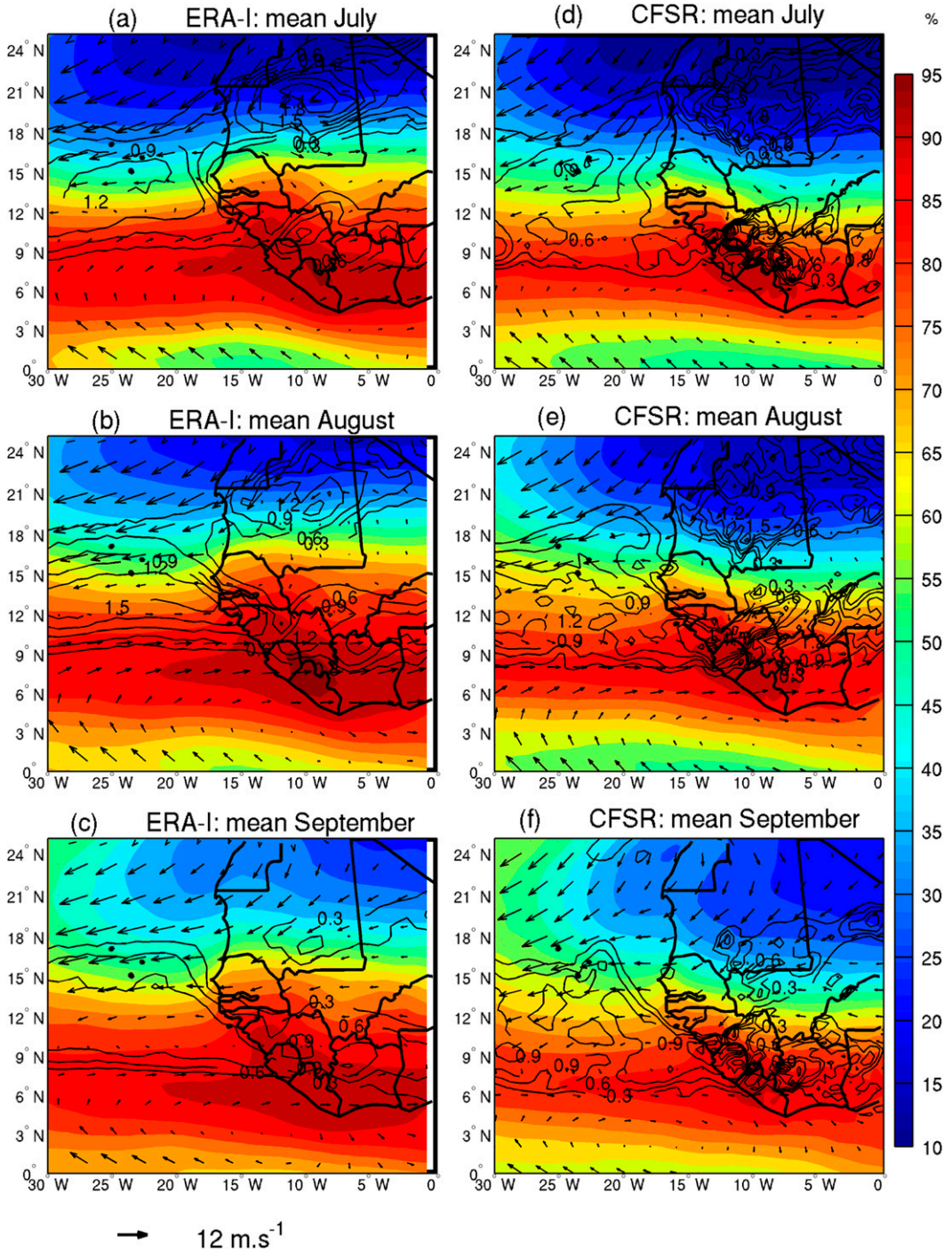

FIG. 4. As in Fig. 3, but for 850 hPa.

(Pytharoulis and Thorncroft 1999; Diedhiou et al. 1999). Hopsch et al. 2007 showed that most of the storms that reach the main development region are driven by the southern AEJ track while storms in the north track often dissipate very shortly after leaving the West African coast.

c. Mean patterns at the ocean surface

Figure 5 shows the mean monthly fields of SST, 10-m surface winds and surface evaporation flux in July (Figs. 5a,d), August (Figs. 5b,e), and September (Figs. 5c,f) for ERA-Interim (left) and CFSR (right). As

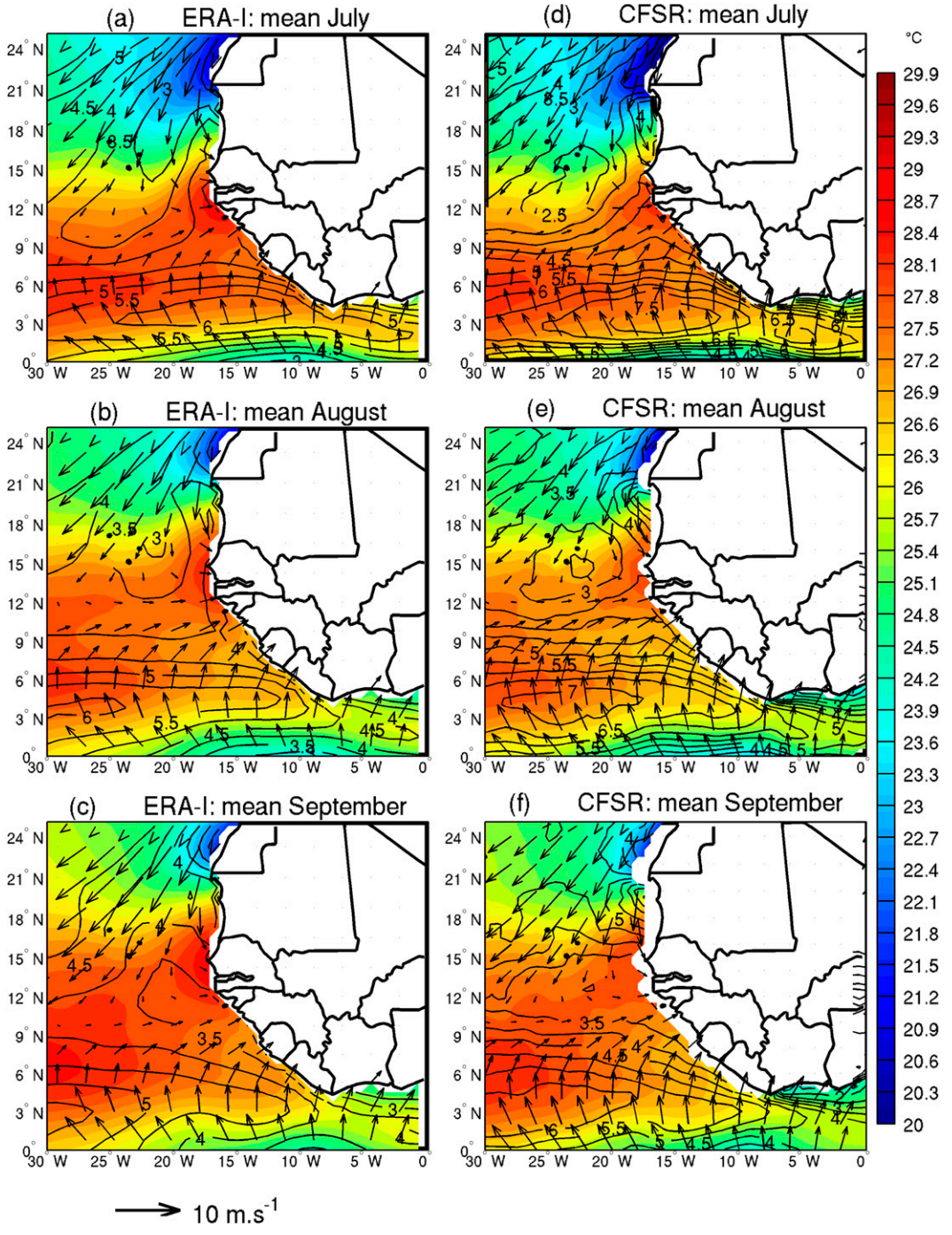

FIG. 5. Mean sea surface temperature (contours, °C), surface wind (arrows, $m\,s^{-1}$), and evaporative flux (contours, $\times 10^{-5}\,kg\,m^{-2}\,s^{-1}$) for (a),(d) July, (b),(e) August, and (c),(f) September for (left) ERA-Interim and (right) CFSR. The fields were only averaged over the years including the dates of selected MCSs.

seen in the previous figures, the northward progression of the ITCZ is associated over the ocean with a northward progression of the maximum SST area (commonly called the warm pool). From July to September this warm pool moves about from 9° to 12°N, shifting the SST gradient toward the north. Southwest and northeast surface winds have the same structure as the winds at 850 hPa. Note that ERA-Interim has a warmer SST than CFSR, whereas CFSR has stronger surface wind and surface evaporation flux. Differences between the two reanalyses are partly due

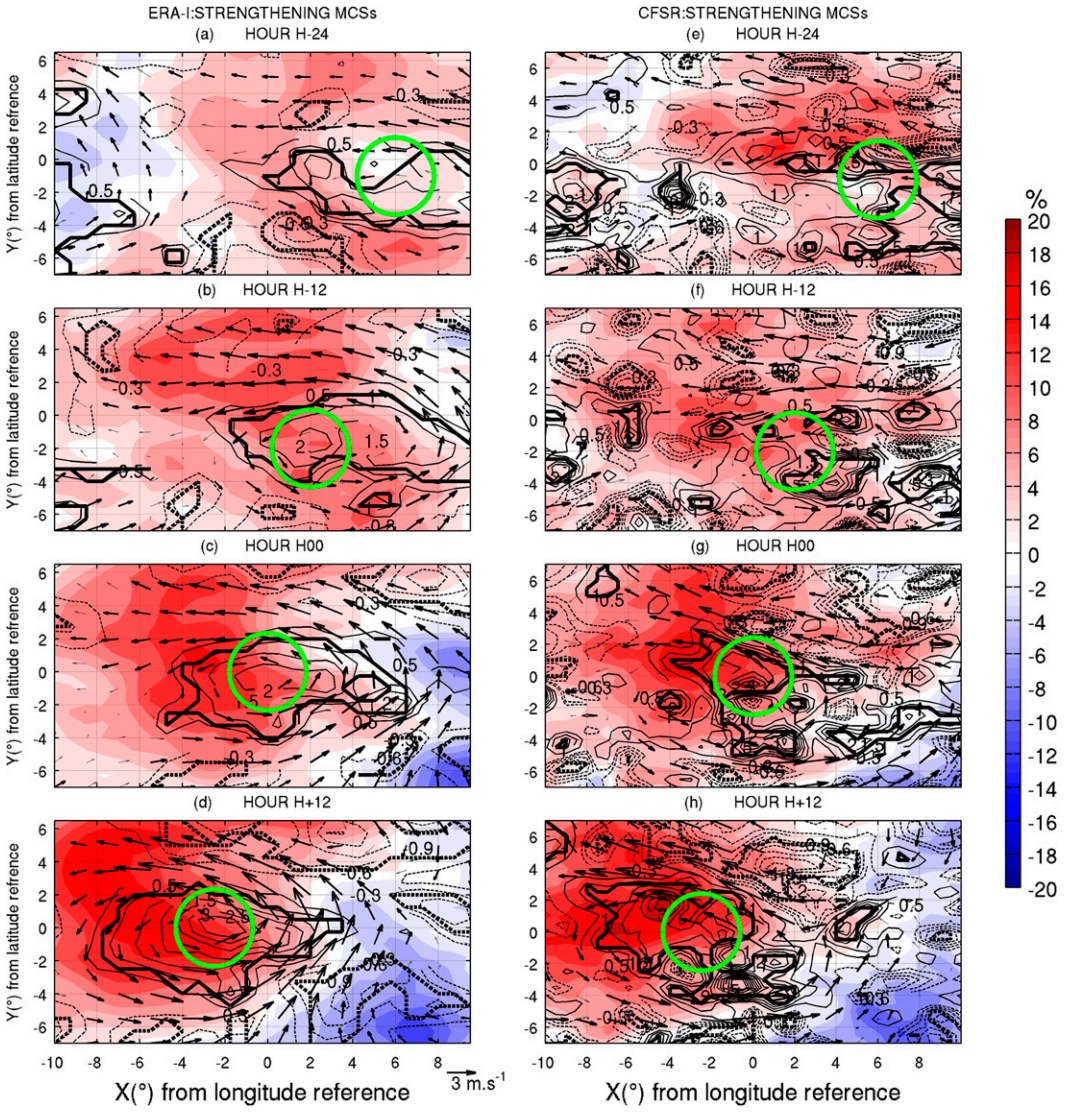

FIG. 6. Composites at 700 hPa of relative humidity anomaly (colors, %), wind anomaly (arrows, m s^{-1}), and relative vertical vorticity anomaly (contours, $\times 10^{-5}$ s^{-1}) at (a),(e) $H-24$ h, (b),(f) $H-12$ h, (c),(g) H00, and (d),(h) $H+12$ h with (left) ERA-Interim and (right) CFSR for strengthening MCSs. Significant values are in bold contours for relative vertical vorticity anomaly and in bold arrows for wind anomaly. The horizontal (vertical) axis (in degrees) is the distance from the reference longitude (latitude). The mean position of the MCS vortex center is indicated by the green circle.

to the different physical parameterizations, but could also be due to ocean–atmosphere coupling in CFSR, contrary to ERA-Interim, as suggested by Leduc-Leballeur et al. (2013), in their study over the Gulf of Guinea.

It is also important to note that the genesis and development of tropical depressions strongly depend on the season. Most tropical cyclones occur in late August to early September (DeMaria et al. 2001), a period during which the SST, low middle-level relative humidity, and relative vorticity are maximized (see Figs. 3–5). In view of this seasonal evolution and to better compare the specific patterns associated to MCS, the composites are calculated using intraseasonal anomalies.

4. Specific characteristics of strengthened and dissipated MCSs

a. Horizontal structures of strengthening MCS

Figure 6 shows composites at 700 hPa of the relative humidity anomaly, relative vorticity anomaly, and wind anomaly with ERA-Interim (left) and CFSR (right). In

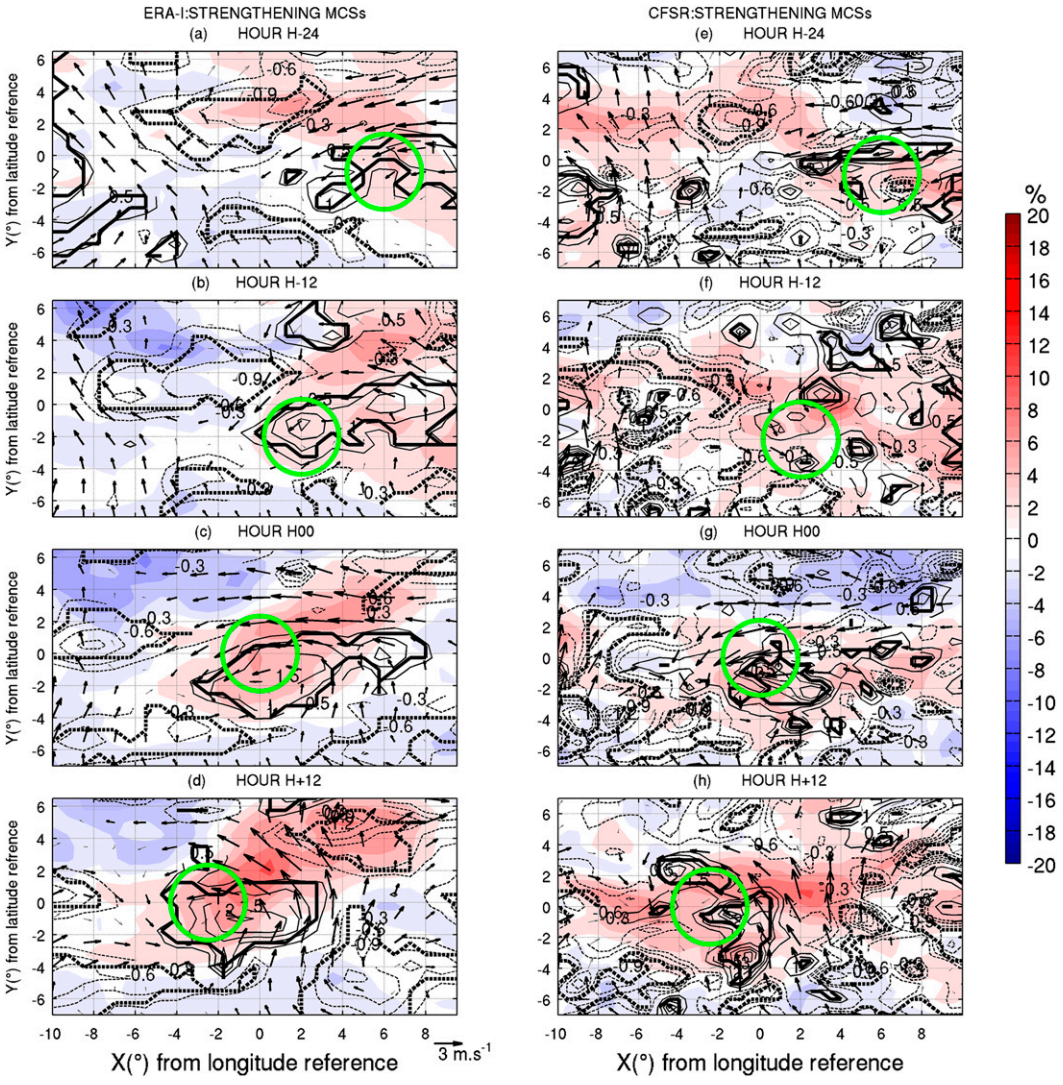

FIG. 7. As in Fig. 6, but at 925 hPa.

both reanalyses, a wide zone of positive relative humidity anomaly occurs in the middle troposphere from $H - 24$ to $H + 12$. However, the cyclonic circulation is clearer in ERA-Interim with a wider diameter of positive relative vorticity, whereas CFSR provides a smaller spatial anomaly pattern. This smaller and scattered pattern could be partly due to its better spatial resolution. At $H - 24$, the vortex center (associated with the MCS system) is centered at (Xref − 6, Yref − 2). From $H - 12$ to $H + 12$, the composite strengthening MCS moves northwestward and the associated anomalies significantly increase in both reanalyses: positive anomalies of relative vorticity increase on average from $+0.5 \times 10^{-5}$ to $+3 \times 10^{-5}\,s^{-1}$, and of relative humidity from +10% to +16% during these 24 h. Note also that the anomaly maximum of relative humidity anomaly is located northwest of the cyclonic vortex. At 925 hPa, the anomalies are weaker than at 700 hPa (Fig. 7). We note the presence of a northward wind anomaly in the oceanic area (between Xref − 10 and Xref) from $H - 24$ to $H - 12$. This anomaly is associated with an increase of the southwesterly wind.

b. *Horizontal structures of dissipating MCS*

For the dissipating case, a positive anomaly of relative humidity is indeed present from $H - 24$ through $H + 12$ at 700 hPa (Fig. 8). However, this anomaly remains small and does not increase, compared to the strengthening case. In addition, a negative relative humidity anomaly is observed on the northwest side of the composite dissipating MCS. The 700-hPa relative vorticity field is almost negative and not significant. The structures at

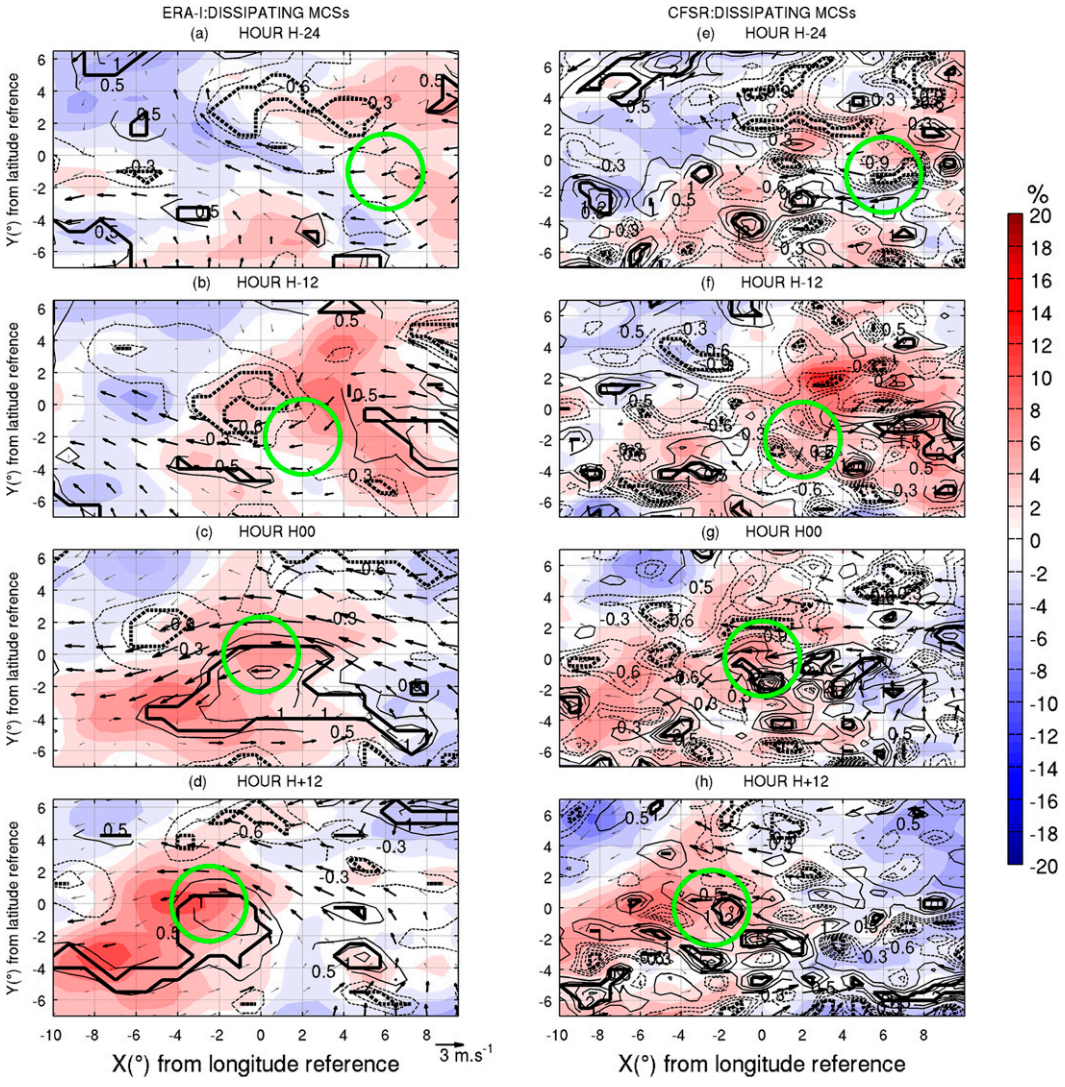

FIG. 8. As in Fig. 6, but showing the composite for dissipative MCSs.

925 hPa are close to those at 700 hPa but with smaller anomalies (not shown).

c. *Vertical structures of strengthening MCS*

Figure 9 shows the zonal–vertical cross section of relative humidity anomaly, wind anomaly, and relative vorticity anomalies of strengthening MCS, from ERA-Interim and CFSR reanalyses. The cross section is obtained by averaging these fields between Yref − 1 and Yref + 1. At $H - 24$, the strengthening MCS, located around Xref + 6 (Figs. 9a,e), is characterized by a high positive relative humidity anomaly (more than +10%) at 500–300 hPa in both reanalyses. A strong positive relative vorticity and vertical velocity anomalies are located just below this relative humidity anomaly. At the same time, significant anomaly of relative humidity is centered at 700 hPa near Xref. It is associated with a positive equivalent potential temperature anomaly (not shown), consistent with convection occurrence. At $H - 12$, the composite MCS continues its westward progression and is near Xref (Figs. 9b,f). Anomalies significantly increase throughout the atmospheric column with a maximum of relative vorticity anomaly in the lower troposphere. Between H00 and $H + 12$, it crosses Xref. The two cores of relative humidity anomalies merge, and the relative vorticity anomaly extends from the surface to the upper troposphere. The convection is enhanced: strong vertical velocities are noted at the center and on the west side of the vorticity anomaly, while subsidence dominates behind the composite MCS. At low and middle levels, strong positive vertical relative vorticity and potential vorticity (PV; not shown)

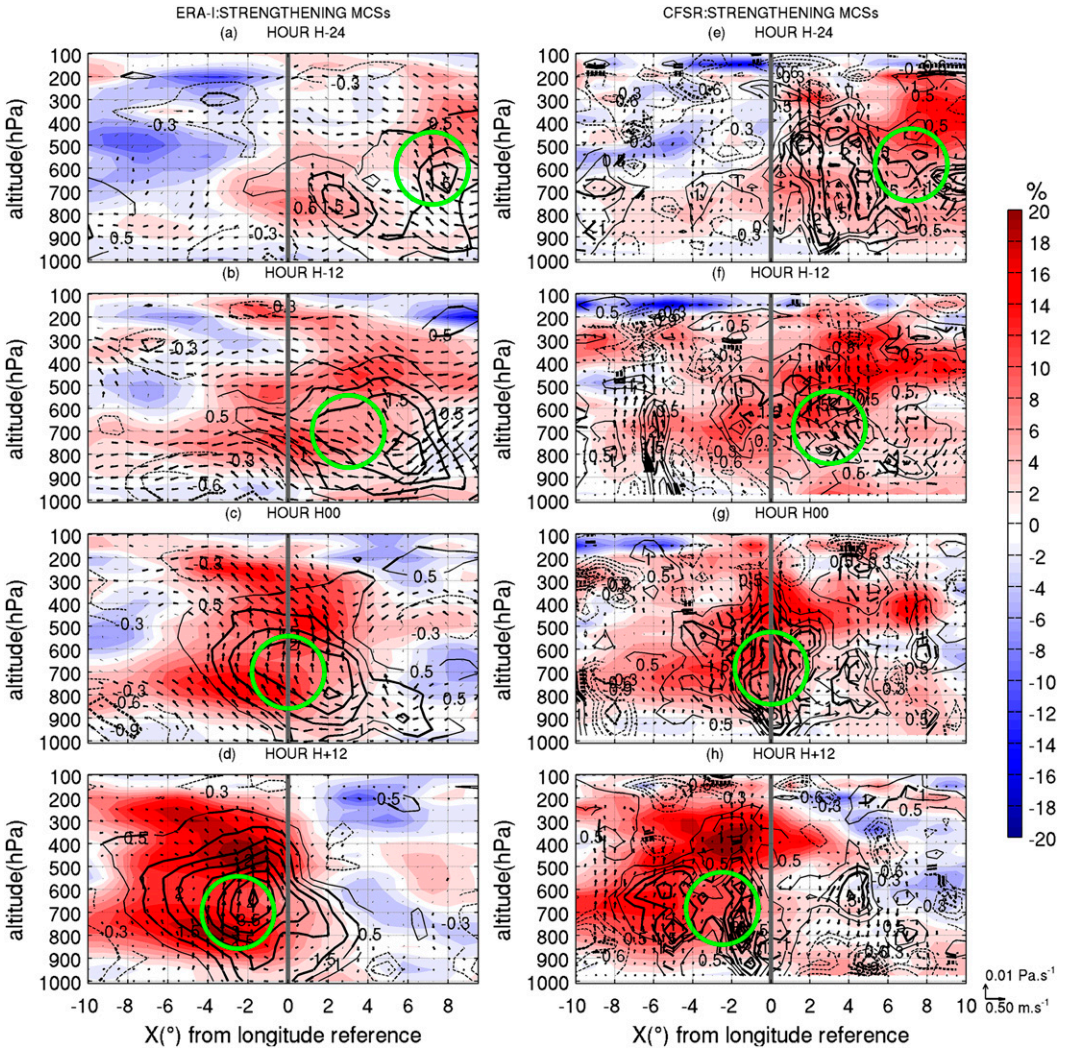

FIG. 9. Zonal–vertical cross sections along the propagation direction (Yref) of MCSs of composite of relative humidity anomaly (colors, %), wind anomaly (arrows, $m\,s^{-1}$), and relative vertical vorticity anomaly (contours, $\times 10^{-5}\,s^{-1}$) at (a),(e) $H-24$ h, (b),(f) $H-12$ h, (c),(g) H00, and (d),(h) $H+12$ h with (left) ERA-Interim and (right) CFSR. The horizontal axis (in degrees) is the distance from the reference longitude. Significant values are in bold contours for the relative vertical vorticity anomaly and in bold arrows for the wind anomaly. The gray line represents the reference longitude.

anomalies develop and at the upper level, the flow becomes divergent (not shown), in agreement with observational and modeling studies for mature MCSs (Raymond and Jiang 1990; Gray 1998; Houze 2004). In addition, dry air is present in the western part of the MCS between 600 and 200 hPa from $H-24$ through $H+12$. It should be noted, however, that the anomalies are more clearly depicted in ERA-Interim than in CFSR.

d. Vertical structures of dissipating MCS

Figure 10 shows the vertical structure for the dissipating case. As in the strengthening case, the dissipating composite MCS is located near Xref + 6 at $H-24$ according to the positive relative humidity anomaly. However, this anomaly is centered near 700 hPa and is collocated with dry air (negative relative humidity anomaly) between 300 and 100 hPa; no significant positive relative vorticity is found. Between $H-12$ and H00, the dissipating composite MCS seems to be slightly enhanced near Xref; however, there is dry air its west side and anticyclonic (negative relative vorticity anomaly) circulation. The presence of dry air could prevent the MCS to further develop. The MCS crosses the coast between H00 and $H+12$. During this period, the ERA-Interim analysis shows a strong eastward acceleration of the zonal wind anomaly between 800 and 500 hPa. This

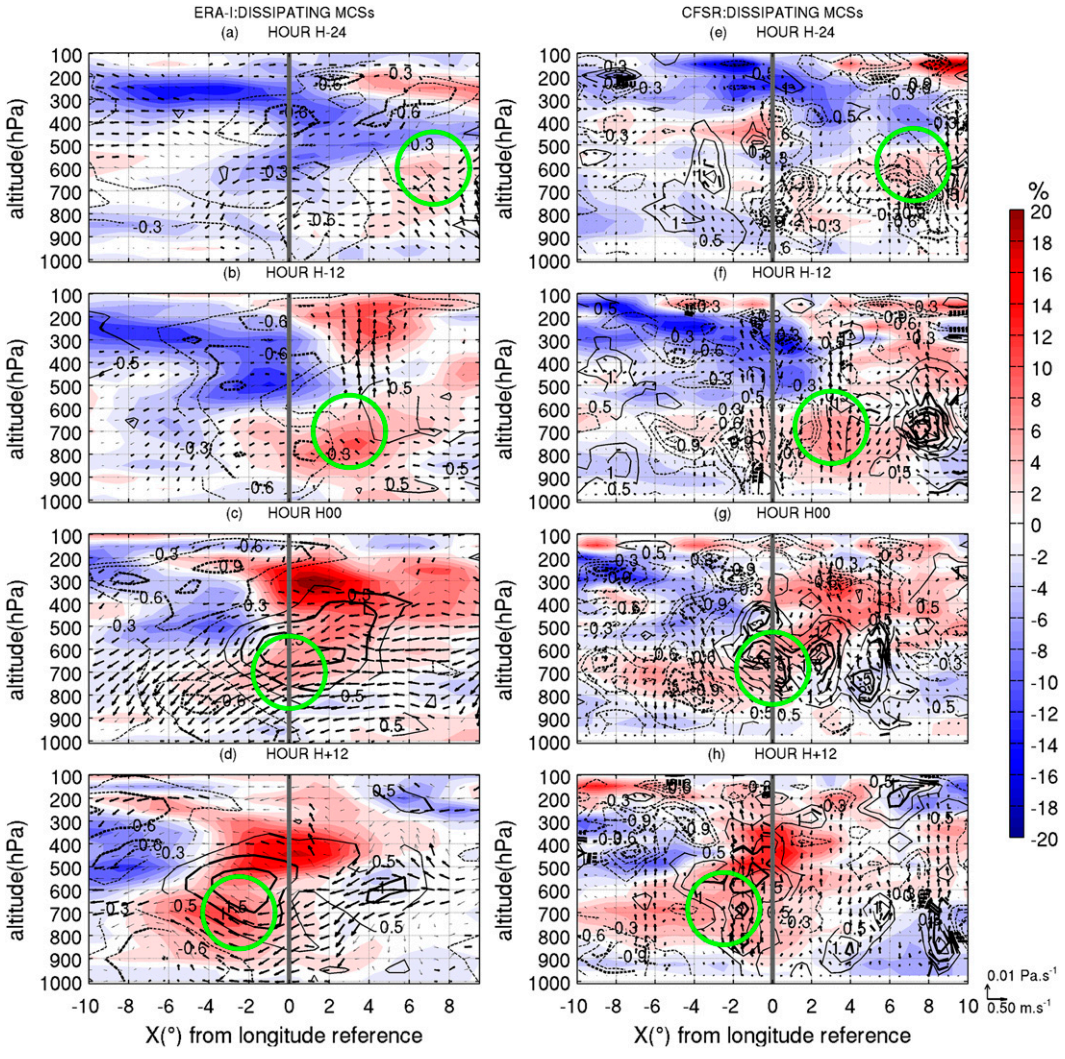

FIG. 10. As Fig. 9, but for dissipative MCS composite.

acceleration could be responsible for vertical gradient of relative humidity and relative vorticity anomalies occurring between the lower and the upper level.

The analysis of horizontal and vertical composite structures shows clear differences between strengthening and dissipating MCS in terms of dynamical organization. Strengthening MCS exhibit a good dynamical organization, consistent with the evolution of mature MCS. In dissipating cases, despite the relative humidity anomaly, which is intrinsically related to the convective system, all the dynamical variables are weak and their evolution does not present significant features. These results are consistent with previous studies (Gray 1998; McBride and Zehr 1981; Zehr 1992; Peng et al. 2012), which showed that large-scale low-level tropospheric winds have significantly larger relative vorticity values in strengthening MCS than in the nondeveloping MCS. Again, ERA-Interim exhibits more coherent structures than CFSR despite the better spatial resolution of CFSR.

Moreover, the relative humidity anomaly is greater at lower levels in the strengthening MCS case. Indeed, high humidity at lower and middle troposphere is important for cyclogenesis because it weakens downdrafts and inhibits the entrainment cooling of updrafts (Bister and Emanuel 1997). The vertical cross section of the strengthening case highlights dynamics and thermodynamics characteristics of a MCS in maturity phase: it has developed a strong middle-level vortex in middle troposphere, and strong vertical velocity and convergence are found on its western flank. When at the coast, the composite strengthening MCS catches up a positive humidity anomaly in the low troposphere. This moisture anomaly at low level, before the arrival of the MCS, is

particularly important because it favors convection and formation of a surface vortex (Sippel et al. 2011). These two anomalies then merge and the MCS quickly intensifies. This result is consistent with Ritchie and Holland (1997) and Simpson et al. (1997), who argued that merging of midlevel mesoscale vortices leads to a greater penetration depth of the circulation, increasing the low-level vorticity.

The vertical cross-sectional analysis also reveals the presence of dry air downstream in both composites between middle to upper troposphere, as observed by Hopsch et al. (2010) and Peng et al. (2012). However, the area of dry air is larger in the dissipating case where anticyclonic circulations and subsiding air are stronger. This result is consistent with Hopsch et al. (2010) and Peng et al. (2012), who found that the nondeveloping AEWs are associated with a prominent dry signal at middle to upper levels, rather than the developing AEWs.

5. Role of African easterly waves with regard to the MCS evolution

a. *Impact of the earlier passage of an AEW trough on the evolution of MCS*

Figure 11 shows the Hovmöller (longitude–time) diagram of CLAUS brightness temperature anomaly and 850-hPa meridional wind anomaly, from ERA-Interim (left) and CFSR (right), for strengthening MCS (top) and dissipating MCS (bottom). Hovmöller diagrams are computed by averaging the fields between Yref − 1 and Yref + 1. The meridional wind is often used to detect and track the westward propagation of AEWs. Here the trough axis is detected as the null value of meridional wind on the diagram, following Fink and Reiner (2003) and Berry and Thorncroft (2005).

In the strengthening case, at Xref, three distinctive troughs can be detected (Figs. 11a,b): a first one at about $H - 72$ (hereinafter labeled T-1), a second one (T0) that is associated with the composite strengthening MCS at about H00, and a third one (T+1) at approximately $H + 84$. The corresponding wave period ranges between two and four days in agreement with previous studies (e.g., Diedhiou et al. 1999, and others). Based on this diagram, the mean phase velocity of the wave at T0 is 9.25 m s^{-1}. This value is consistent with Fink and Renier, who estimated a value of AEW propagation speed of 9.1 m s^{-1}.

The 850-hPa meridional wind anomaly, in the Hovmöller diagram of the composite dissipating MCS, is too weak and noisy but we can note the presence an AEW trough at $H + 24$ (after passage of the dissipating composite MCS) in both reanalyses (Figs. 11c,d). No preceding AEW trough with clear convective activity is found on this diagram. The horizontal cross section at 850 hPa (Fig. 13) shows that the dissipating MCS begins to enter in an anticyclonic circulation at $H - 18$ and is fully in it at H00. The weak and noisy signal of meridional wind anomaly noted in this case could be the result of over imposition of different individuals AEW sectors.

In the following, we will only focus on T-1 and T0 (before and during the coast overpass by the strengthening MCS). Figure 12 shows the composite horizontal map at 850 hPa of brightness temperature and wind anomalies at $H - 18$ and $H + 12$ for both reanalyses. This pressure level is chosen to examine the wave structure, because it was established by Carlson (1969) and Thorncroft and Hodges (2001) that a cyclonic wind is associated with an AEW trough. Thus we examine how this previous cyclonic circulation anomaly related to T-1 may be related with the low-level circulation downstream from the strengthening MCS associated with T0. At $H - 18$, T-1 (center of the first cyclonic circulation) is located at Xref − 13; T0 is over the continent near Xref + 7. The corresponding wavelength is then approximately 2000 km. This wavelength value is slightly smaller than the mean wavelength of most AEWs (between 2500 and 4000 km), as it results from wave contraction over the ocean, as noted in earlier studies (Reed et al. 1977; Kiladis et al. 2006; Diedhiou et al. 2001). From $H - 18$ to $H + 12$, T-1 moves to Xref − 20 and T0 moves to Xref + 4. The mean distance between the two troughs is now approximately 1600 km, since T0, being over the continent, moves faster than T-1. Between the two troughs there occurs a positive relative humidity anomaly associated with a strong wind convergence anomaly (not shown). These anomalies could be favored by the presence of the trough T-1, through southerly/southwesterly wind enhancement.

The strengthening composite patterns agree with Vizy and Cook (2009), who found that the formation of Tropical Depression Debby (August 2006) over the Cape Verde region was preceded by a wave associated with the genesis of the Ernesto depression in the western Atlantic. They argued that the passage of the AEW that later developed into Ernesto was a factor that preconditioned the lower troposphere, making the environment favorable for the development of the Debby-associated wave by enhancing low-level southwesterly flow, convergence, horizontal low-level zonal shear, and cyclonic relative vorticity ahead of Debby. In their case study, the AEW (which was further associated with the tropical depression pre-Ernesto) was downstream, approximately 2000 km to the west of the Debby vortex. Our composite analysis generalizes this particular case analysis to 18 strengthening MCS cases (see Tables 2 and 3): these strengthening MCSs, embedded in AEWs, are preceded by previous AEW troughs, associated with

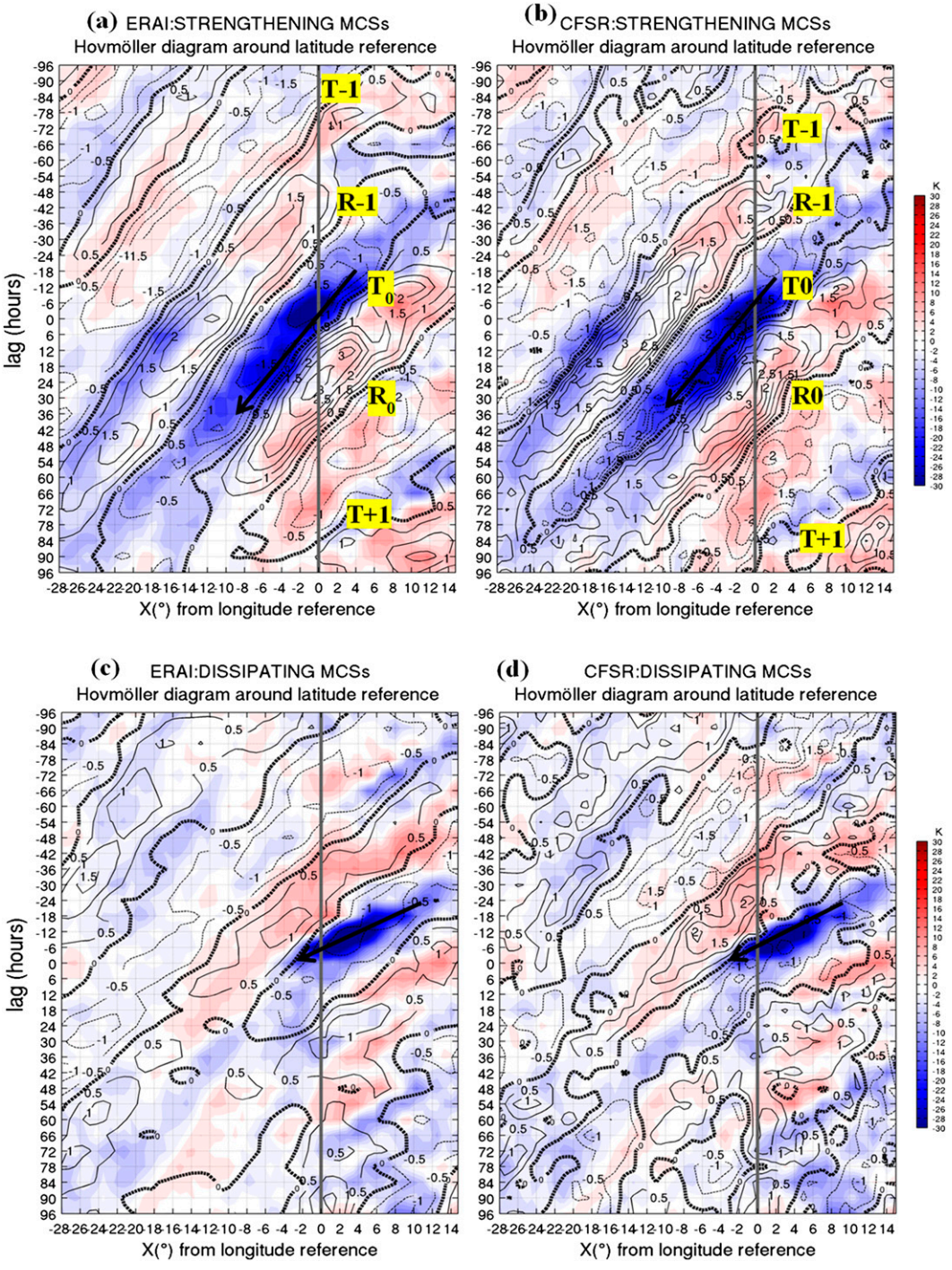

FIG. 11. Hovmöller diagram of brightness temperature anomaly (colors, K) and 850-hPa meridional wind anomaly (contours, m s^{-1}) with (left) ERA-Interim and (right) CFSR for the (a),(b) strengthening and (c),(d) dissipating MCS composite. The vertical gray line is the reference longitude, and T (R) shows the trough (ridge) wave position. The bold black arrow shows the approximate propagation direction of the MCS composite.

a strong cyclonic vorticity at low levels and significant convective activity behind. These previous AEWs trough could bring humidity to the strengthening MCSs from their southeast flank.

b. MCS location with respect to the wave sector

In the strengthening MCS case, as shown by the brightness temperature anomaly field, significant convection

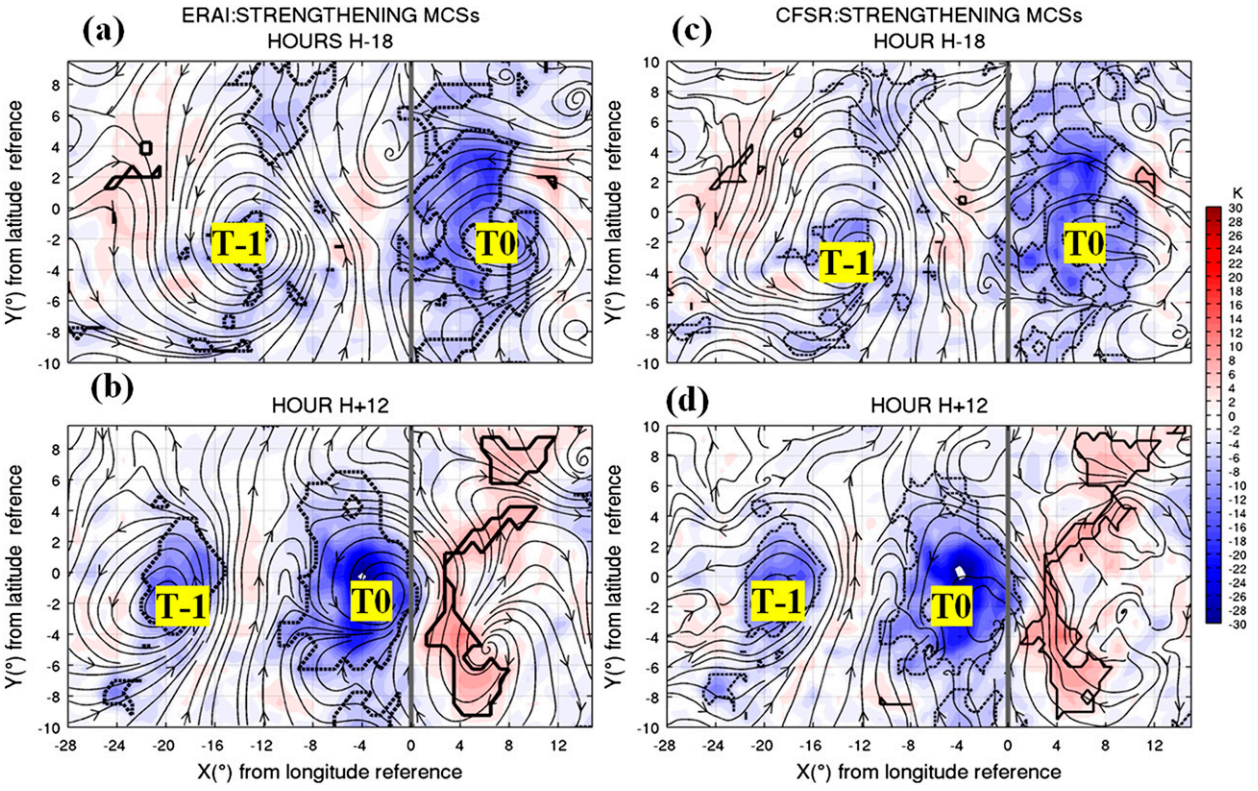

FIG. 12. Composites of brightness temperature anomaly (colors, K) and 850-hPa wind anomaly (streamlines and vectors) at (top) $H - 18$ and (bottom) $H + 12$ for strengthening MCSs with (a),(b) ERA-Interim and (c),(d) CFSR. Significant values are in black contours for brightness temperature anomaly; T-1 and T0 show the previous and the main AEW trough positions, respectively (see text for details).

(negative anomaly) develops in the south sector of the previous trough T-1, while near the reference longitude the strengthening MCS evolves between the second trough T0 and the north sector of the AEW (Figs. 11a,b and 12). The presence of convection behind the first trough over ocean agrees with Kiladis et al. (2006).

Figures 11c and 11d show that the composite dissipating MCS is located in the north sector of an AEW trough and but that it moves more quickly than the wave, so it catches up the ridge sector wherein it dissipates a few hours after reaching the longitude reference. Figures 13c and 13d confirm that it is embedded in a strong anticyclonic circulation when dissipation occurs.

Thus, the Hovmöller diagrams and the horizontal cross section at 850 hPa of composites show that, on average, strengthening MCSs are located near the north sector of the trough axis, whereas dissipating MCS lie mainly between the north sector and the ridge. To evaluate the robustness of these results, all 40 MCSs were individually checked, with their associated AEWs, using CLAUS brightness temperatures and ERA-Interim wind fields, following the method described in Fink and Reiner (2003). Table 2 shows the overall results of this analysis:

- 11 strengthening MCS cases are found within the trough area;
- 8 dissipating MCS take place in the ridge area; and
- no MCS lying close to the ridge axis is reinvigorated.

These results are consistent with Hopsch et al. 2010, who established, using a composite analysis, that deep convection is located in the vicinity of the trough when AEWs strengthen near the West African coast. The trough region axis of AEW is often favorable for MCS enhancement because the system can benefit of additional relative

TABLE 2. Number of MCSs observed in different sectors of AEWs at the coast.

	MCS in the vicinity of the north sector	MCS in the vicinity of the trough sector	MCS in the vicinity of the south sector	MCS in the vicinity of a ridge	Total of MCSs with previous AEW trough
Strengthening MCS	7/20	11/20	2/20	0/20	18/20
Dissipating MCS	6/20	2/20	4/20	8/20	6/20

TABLE 3. Number of MCSs associated with preceding AEW trough.

	MCSs in the vicinity of the north sector with previous AEW trough	MCSs in the vicinity of the trough sector with previous AEW trough	MCSs in the vicinity of the south sector with previous AEW trough	MCSs in the vicinity of the ridge sector with previous AEW trough	Total of MCSs with previous AEW trough
Strengthening MCS	6/18	10/18	2/18	0/18	18/20
Dissipating MCS	3/6	0/6	0/6	3/6	6/20

positive vorticity from the AEW (Fink and Reiner, 2003). The large number (8/20) of MCSs that dissipate in the vicinity of ridge sector is also consistent with Fink and Reiner (2003), who found, over the entire West African region, that 40% of decayed MCSs occur in the vicinity of a ridge. Indeed, MCS often decay when they are in the vicinity of the ridge axis because this region is characterized by anticyclonic and dry subsiding air (e.g., Reed et al. 1977; Diedhiou et al. 1999; Fink and Reiner, 2003; Kiladis et al. 2006). Furthermore, the 700-hPa flow circulation anomaly associated with the composite dissipating MCS (Fig. 8) is almost anticyclonic, confirming that dissipating cases are associated mostly with the ridge sector (anticyclonic rotation). Therefore, the phase relationship between the location of MCS and the trough or ridge sector seems to be an important dynamical factor for the evolution of the convective systems off the West African coasts.

However, we note that approximately the same number of MCSs either reinvigorated (7/20) or dissipated (6/20) in the north sector of the AEW. But as shown in the Hovmöller diagrams, the dissipating MCSs appear to move faster than their associated wave so they can quickly leave the north sector to reach the ridge sector where they

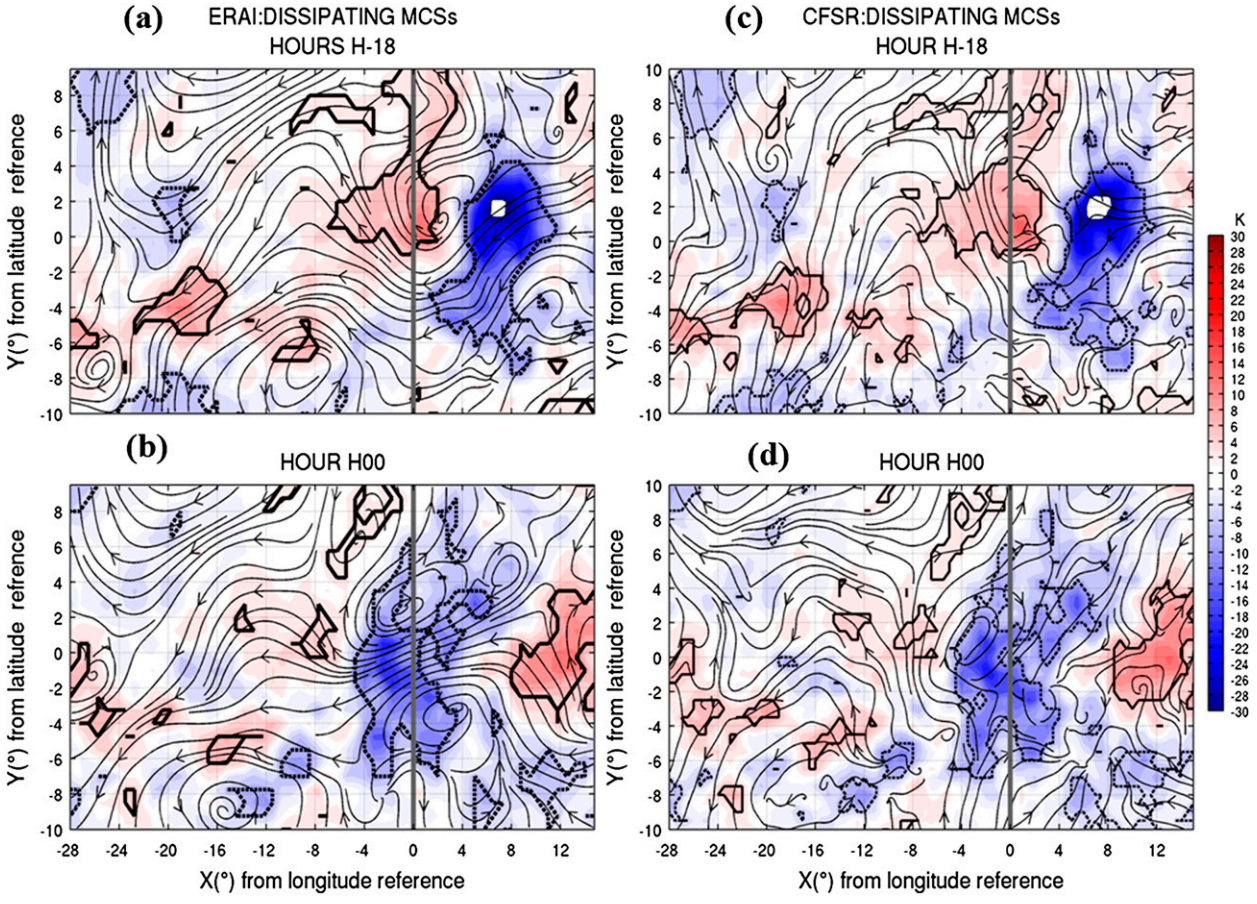

FIG. 13. Composites of brightness temperature anomaly (colors, K) and 850-hPa wind anomaly (streamlines and vectors) at (top) $H-18$ h and (bottom) H00 for dissipating MCSs with (a),(b) ERA-Interim and (c),(d) CFSR. Significant values are in black contours for brightness temperature anomaly.

dissipate. On the contrary, strengthening MCSs, moving in phase with the wave, stay in the north sector. This result is supported by the results of Peng et al. (2012), who show that developing disturbances, one day prior to tropical depression genesis in the north tropical Atlantic, have a significantly slower speed than nondeveloping disturbances.

Finally, the two dissipating MCS found in the vicinity of the AEW trough are not preceded by a previous AEW trough (Tables 2 and 3). This may explain why they did not develop.

6. Surface oceanic conditions and air–sea interactions

We found that the preceding AEW trough could play a key role in the strengthening MCS composite, since the associated cyclonic vortex could enhance the southwesterly flow. To evaluate the water vapor transfers around the MCS, this section analyses the humidity fluxes in the low atmosphere and from the surface.

The dissipating case is not, on average, associated with a preceding AEW trough. Moreover, no significant vertical integration of specific humidity in the surface–850-hPa layer is observed when it crosses the reference longitude (not shown). Also, the moisture flux convergence integrated in the surface–850-hPa layer is not significant (not shown). Therefore only results from strengthening MCS composite will be shown in this section.

a. *Surface oceanic conditions*

Figure 14 shows composites of the SST anomaly, surface–850-hPa integrated specific humidity anomaly, and 10-m surface wind anomaly from $H-24$ to $H+24$ for strengthening MCSs with ERA-Interim (left) and CFSR data (right). From $H-24$ to $H-12$, over the ocean, the southwesterly wind strengthens, while the northeasterly wind weakens. The southwesterly wind increases are more sustained in the CFSR reanalysis. Negative (positive) anomaly of SST slightly increases [of about 0.1°C to the south (north) of Yref]. The MCS crosses Xref between $H-12$ and $H+12$ while the surface cyclonic vortex begins to form. Between $H+12$ and $H+24$ it moves toward the northwest, being associated with a significant increase in integrated specific humidity. The SST anomaly slightly decreases in ERA-Interim and does not change in in CFSR.

b. *Interaction with the ocean surface*

Following Cadet and Nnoli (1987) and Thorncroft et al. (2011), the moisture fluxes and the moisture flux convergence fields are computed at each grid point of reanalyses using the following equations:

$$Fv = \frac{1}{T}\int_0^T -\frac{1}{g}\left(\int_{\mathrm{Pb}}^{\mathrm{Pt}} qu\,dp\right)dt, \tag{1}$$

$$Q = \frac{1}{T}\int_0^T \frac{1}{g}\left(\int_{\mathrm{Pb}}^{\mathrm{Pt}} \nabla\cdot qu\,dp\right)dt, \tag{2}$$

with g being the acceleration of gravity, q the specific humidity, u the wind component, p the pressure, Pb and Pt the pressures at the bottom and at the top of the layer, and T the averaging period. Equation (1) gives the moisture fluxes (F_v) and Eq. (2) gives the moisture flux convergence fields (Q). Cadet and Nnoli (1987) showed that the moisture flux at middle layers (related to the African easterly jet) plays a minor role in the moisture flux convergence in the Sahelian and the eastern Atlantic regions, so the fields are only computed in the lower layers (between the surface and 850 hPa).

Figure 15 shows composite maps of the surface evaporation flux, moisture flux convergence (contours), and moisture flux anomalies (vectors). At $H-24$ (Figs. 15a,f), while the strengthening MCS is over the continent (around Xref − 6), the cyclonic circulation associated with the previous AEW trough (T-1) induces a northward humidity flux anomaly on its eastern side over the ocean. At the surface, the evaporation flux is increased (decreased) in the south (north) zone from the reference latitude. Between $H-12$ and $H+12$ (Figs. 15b,c,g,h), both systems continue their westward displacement, but the composite strengthening MCS and its associated AEW trough, moving faster than the first AEW trough, becomes closer to it can benefit from the increased southwesterly flux. A significant moisture flux convergence anomaly (between 15×10^{-5} and $20\times10^{-5}\,\mathrm{kg\,m^{-2}\,s^{-1}}$) is located downstream from the strengthening MCS during this period. After $H+12$, the strengthening MCS seems to slow down over the ocean. Note that there is a positive surface evaporation flux anomaly increase in CFSR. The evaporation flux anomaly is, during this phase, greater in CFSR than in ERA-Interim, possibly because of the ocean–atmosphere model coupling, which enables an interactive ocean response to the atmosphere perturbation. At $H+24$, the composite strengthening MCS becomes stronger and could take enough energy from the sea to become energetically self-sustained (Emanuel 1986).

7. Discussion

We have found that the southwesterly surface wind increase in the south area of the ocean region occurs during the same time as the first AEW trough takes place in this region. During the same time, the surface evaporation flux increases in the south area and decreases in the north area with respect to the reference latitude (Fig. 15). Indeed, the surface wind increase induces an enhancement of the surface evaporation flux, which results in a decrease of

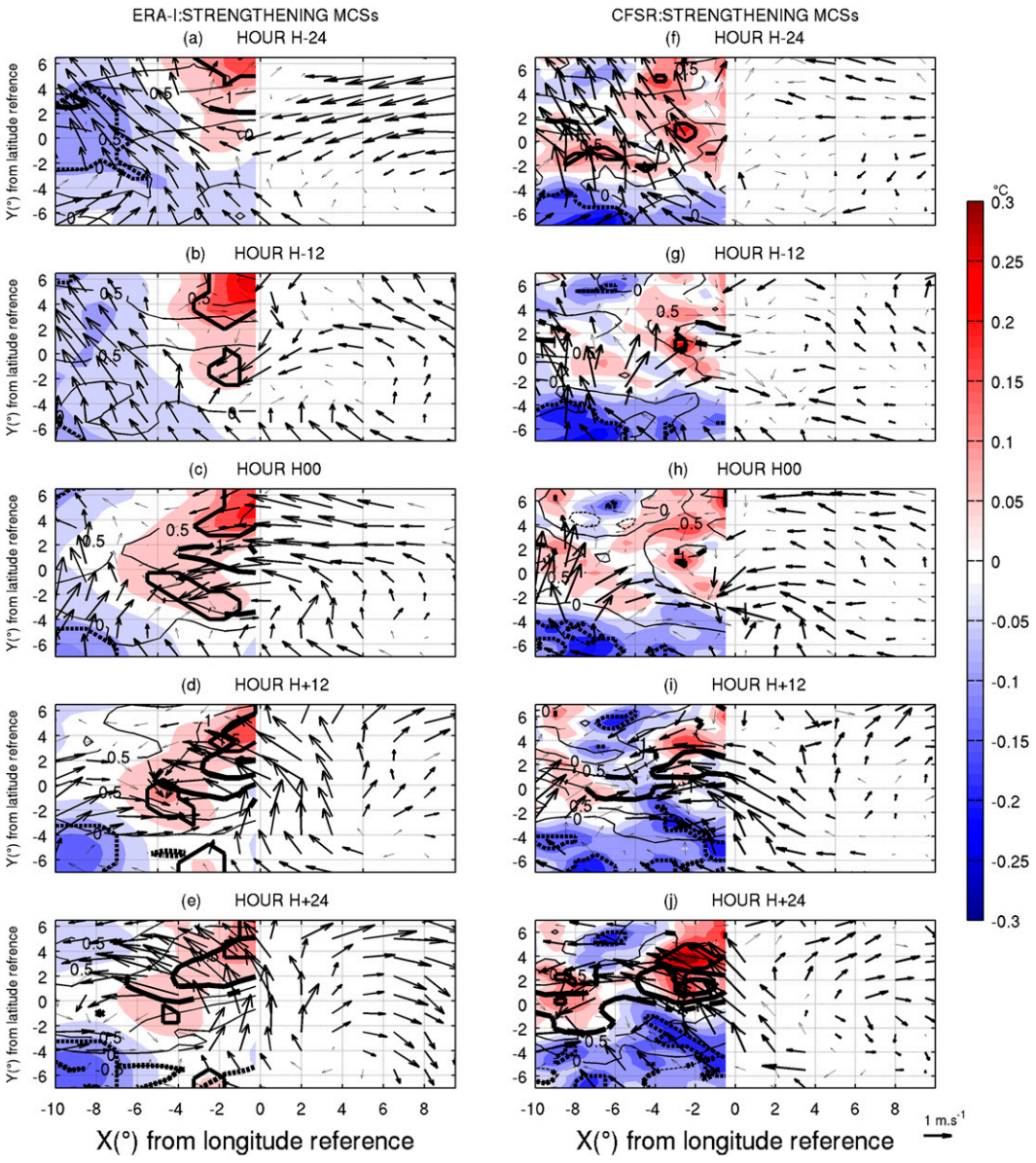

FIG. 14. Strengthening MCSs composite case: composite of SST anomaly (colors, °C), anomaly of the vertical integration of specific humidity in the surface–850 hPa layer (contours, kg m^{-2}), and surface wind anomaly (arrows, m s^{-1}) at (a),(f) $H - 24$ h, (b),(g) $H - 12$ h, (c),(h) H00, (d),(i) $H + 12$ h, and (e),(j) $H + 24$ h with (left) ERA-Interim and (right) CFSR. Significant values are in black bold contours for the SST anomaly and in bold arrows for the surface wind anomaly.

the SST (Small et al. 2008). The opposite is observed when the surface wind is decreasing. Thus, the SST cooling (warming) noted in the south (north) could be a result of dynamical forcing by the first AEW trough on the SST, through the acceleration (slowing down) of the southwesterly (northeasterly) surface wind. In addition, we note with CFSR that the positive surface evaporation flux strongly increases when the strengthening MCS crosses the positive SST anomaly (Fig. 14), and the surface–850-hPa integrated specific humidity anomaly quickly increases (Fig. 15) from H00 to $H + 24$.

By looking at the moisture fluxes and of moisture flux convergence anomalies, it is clear that the previous AEW trough significantly contributes to the development of the strengthening MCS by providing humidity in lower layers. This humidity supply is rendered effective through the combination of three factors:

- The first AEW trough is associated with significant convection activity and a strong cyclonic vortex at middle and low layers, allowing it to enhance the southwesterly flow, east of its location.

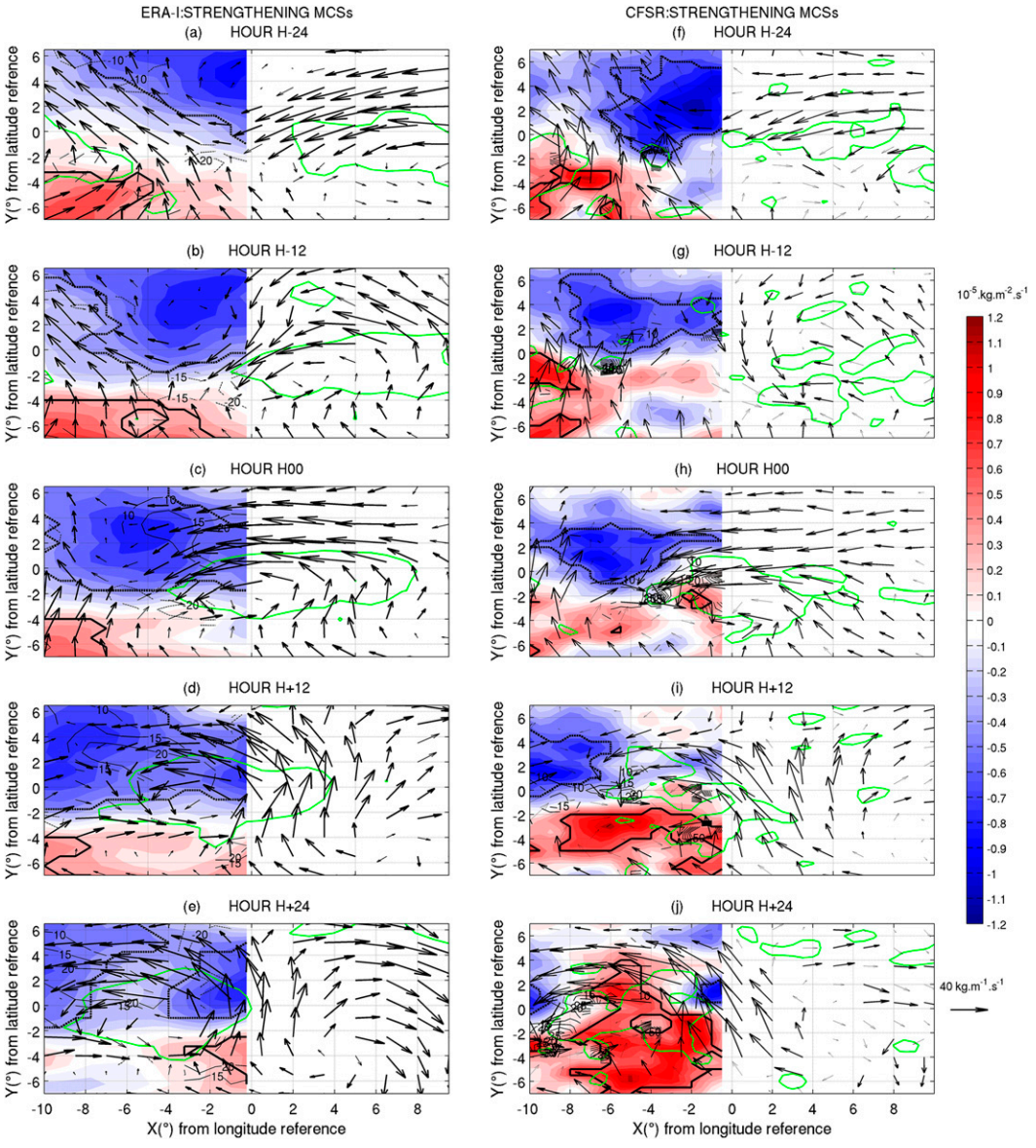

FIG. 15. Strengthening MCSs case: composites of evaporation flux anomaly (colors, $\times 10^{-5}$ kg m^{-2} s^{-1}), anomaly of the vertical integration flux of specific humidity in the surface–850-hPa layer (arrows, kg m^{-1} s^{-1}), and moisture flux convergence anomaly (contours, $\times 10^{-5}$ kg m^{-2} s^{-1}; only significant values are outlined) at (a),(f) $H - 24$ h, (b),(g) $H - 12$ h, (c),(h) H00, (d),(i) $H + 12$ h, and (e),(j) $H + 24$ h for (left) ERA-Interim and (right) CFSR. Green contours show the systems track based on its 850-hPa relative vorticity anomaly. Significant values are in black bold contours for the evaporation flux anomaly and in bold arrows for the anomaly of the vertical integration flux of specific humidity in the surface–850-hPa layer.

- The contraction of the wavelength makes the strengthening MCS composite to become closer to the first AEW trough and thus to benefit from the humidity flux generated by its cyclonic circulation.
- Both systems evolve in the same latitude band.

Indeed, according to Gray (1998), the presence or absence of a wind burst is a crucial factor in the tropical cyclone formation. Such a wind burst can be initiated by wind surges in the trade winds, southwesterly monsoon flow, or wind convergence resulting from easterly wave–induced convergence. By inducing convergence, the wind surge can trigger convection if it occurs at the place where a convective vortex has previously developed. Briegel and Frank (1997) objectively analyzed tropical cyclones forming in the western Pacific monsoon trough at two different levels, 850 and 200 hPa, for the years 1988 and 1989 to explore the relationships between

large-scale forcing and tropical cyclogenesis. Their analysis revealed that low-level southwesterly wind surges occur southwest of the cyclone generation location approximately 48–72 h prior to genesis. They argued that these wind surges could force the low-level convergence and deep convection necessary for tropical cyclogenesis in this region. Similarly, our results show that wind bursts can be triggered and maintained by the prior AEW trough, also confirming Vizy and Cook (2009), in the fact the strengthening MCS is supplied by humidity from the first one. In addition, our results suggest that the previous system interacts with the oceanic surface, enhancing the evaporation, which can then be advected toward the strengthening MCS by the northward surface wind anomaly.

8. Conclusions

This study compares strengthening and dissipating MCS structures and ocean–atmosphere features prevailing when they leave the West African coast. Radar, MSG, and CLAUS data were used to select and monitor MCS cases in this coastal region. A lagged composite analysis, of which the significance is statistically evaluated using a Monte Carlo test, is then performed for the two sets (20 strengthening and 20 dissipating MCSs) using ERA-Interim and CFSR reanalyses. During their westward motion over the ocean, several important characteristics can be pointed out in the two cases.

From $H - 24$ to $H - 12$ h, the composite strengthening MCS is located in the vicinity of an AEW trough, while the previous trough, associated with significant convective activity behind its center, is close to the coast. This first trough is associated with a cyclonic circulation in the low troposphere, strengthening the southwesterly flow, which provides a moisture flux to the strengthening MCS. This supply is maximal when the strengthening MCS becomes closer to the first AEW trough. Both the wavelength contraction and their similar trough latitude probably facilitate the moisture supply. Near the surface, the first AEW trough induces a wind surface increase in it southeast side and a decreasing surface wind northeast of its center. It results in a SST cooling in the south part and a SST warming in the north, suggesting that the SST plays a role in the lower-layer humidification in the strengthening MCS on its south through upward surface evaporation flux. However, this contribution is smaller than the southwest humidity advection flux. During the coast overpass (from H00 to $H + 12$), the strengthening MCS crosses the warmer SST area caused by the passage of the previous AEW trough, while surface evaporation flux and the surface–850-hPa integrated specific humidity anomaly quickly increases.

Contrary to the strengthening case, the dissipating composite MCS moves in a dry environment associated with subsiding air and with anticyclonic circulation.

Examination of individual MCSs confirm that most of the strengthening MCSs are in the trough region of an AEW with a preceding trough, while the dissipating MCS are often in the vicinity of the ridge region and are not influenced by a previous AEW trough. Therefore, the phase relationship between the location of MCS and the trough or sector ridge sector and also the presence or absence of a previous AEW trough seem to be important factors for the evolution of the convective systems off the West African coasts.

However, these factors must not be considered as sufficient conditions for MCS evolution in that region, which also depends on several others environmental conditions that are not examined in this work. But we suggest that they could significantly increase the likelihood for a system that just crossed the coast to be maintained and developed over the eastern tropical Atlantic region, and have implications for a much more wide-ranging analysis. The use of numerical modeling would possibly allow for better quantification of the effect of a previous AEW trough and better clarification of the role of the SST with regard to the strengthening MCS near the West African coast.

Acknowledgments. We thank Gregory Jenkins and two anonymous reviewers for their comments on the manuscript. The reanalyses and CLAUS data were obtained from the Institut Pierre Simon Laplace (IPSL; http://www.ipsl.fr/). Meteosat imagery was provided by AMMA. Radar data were provided by the ''Agence Nationale de l'Aviation Civile et de la Météorologie du Sénégal'' (ANACIM). This work was funded by the Agence Universitaire de la Francophonie.

REFERENCES

Arnault, J., and F. Roux, 2010: Comparison between two case studies of developing and nondeveloping African easterly waves during NAMMA and AMMA/SOP-3: Absolute vertical vorticity budget. *Mon. Wea. Rev.,* **138,** 1420–1445, doi:10.1175/2009MWR3120.1.

——, and ——, 2011: Characteristics of African easterly waves associated with tropical cyclogenesis in the Cape Verde islands region in July–August–September of 2004–2008. *Atmos. Res.,* **100,** 61–82, doi:10.1016/j.atmosres.2010.12.028.

Berry, G., and C. D. Thorncroft, 2005: Case study of an intense African easterly wave. *Mon. Wea. Rev.,* **133,** 752–766, doi:10.1175/MWR2884.1.

Bister, M., and K. A. Emanuel, 1997: The genesis of Hurricane Guillermo: TEXMEX analyses and a modeling study. *Mon. Wea. Rev.,* **125,** 2662–2682, doi:10.1175/1520-0493(1997)125<2662:TGOHGT>2.0.CO;2.

Briegel, L. M., and W. M. Frank, 1997: Large-scale influences on tropical cyclogenesis in the western North Pacific. *Mon. Wea. Rev.,* **125,** 1397–1413, doi:10.1175/1520-0493(1997)125<1397:LSIOTC>2.0.CO;2.

Cadet, D. L., and N. O. Nnoli, 1987: Water vapour transport over Africa and the Atlantic Ocean during summer 1979. *Quart. J. Roy. Meteor. Soc.,* **113,** 581–602, doi:10.1002/qj.49711347609.

Carlson, T. N., 1969: Synoptic histories of three African disturbances that developed into Atlantic hurricanes. *Mon. Wea. Rev.,* **97,** 256–276, doi:10.1175/1520-0493(1969)097<0256:SHOTAD>2.3.CO;2.

Chiao, S., and G. S. Jenkins, 2010: Numerical investigations on the formation of Tropical Storm Debby during NAMMA-06. *Wea. Forecasting,* **25,** 866–884, doi:10.1175/2010WAF2222313.1.

Dee, D. P., and Coauthors, 2011: The ERA-Interim reanalysis: Configuration and performance of the data assimilation system. *Quart. J. Roy. Meteor. Soc.,* **137,** 553–597, doi:10.1002/qj.828.

DeMaria, M., J. A. Knaff, and B. H. Connell, 2001: A tropical cyclone genesis parameter for the tropical Atlantic. *Wea. Forecasting,* **16,** 219–233, doi:10.1175/1520-0434(2001)016<0219:ATCGPF>2.0.CO;2.

Diedhiou, A., S. Janicot, A. Viltard, P. de Felice, and H. Laurent, 1999: Easterly wave regimes and associated convection over West Africa and tropical Atlantic: Results from the NCEP/NCAR and ECMWF reanalyses. *Climate Dyn.,* **15,** 795–822, doi:10.1007/s003820050316.

——, ——, ——, and ——, 2001: Composite patterns of easterly disturbances over West Africa and the tropical Atlantic: A climatology from the 1979–95 NCEP/NCAR reanalyses. *Climate Dyn.,* **18,** 241–253, doi:10.1007/s003820100173.

Dunion, J. P., and C. S. Velden, 2004: The impact of the Saharan air layer on Atlantic tropical cyclone activity. *Bull. Amer. Meteor. Soc.,* **85,** 353–365, doi:10.1175/BAMS-85-3-353.

Emanuel, K. A., 1986: An air–sea interaction theory for tropical cyclones. Part I: Steady-state maintenance. *J. Atmos. Sci.,* **43,** 585–605, doi:10.1175/1520-0469(1986)043<0585:AASITF>2.0.CO;2.

Fink, A. H., and A. Reiner, 2003: Spatiotemporal variability of the relation between African easterly jets and West African squall lines in 1998 and 1999. *J. Geophys. Res.,* **108,** 4332, doi:10.1029/2002JD002816.

Goldenberg, S. B., and L. J. Shapiro, 1996: Physical mechanisms for the association of El Niño and West African rainfall with Atlantic major hurricanes. *J. Climate,* **9,** 1169–1187, doi:10.1175/1520-0442(1996)009<1169:PMFTAO>2.0.CO;2.

——, C. W. Landsea, A. M. Mestas-Nuñez, and W. M. Gray, 2001: The recent increase of Atlantic hurricane activity: Causes and implications. *Science,* **293,** 474–479, doi:10.1126/science.1060040.

Gray, W. M., 1975: Tropical cyclone genesis. CSU Dept. of Atmospheric Science Paper 234, Colorado State University, 121 pp.

——, 1979: Hurricanes: Their formation, structure and likely role in the tropical circulation. *Meteorology over the Tropical Oceans,* D. B. Shaw, Ed., Royal Meteorological Society, 155–218.

——, 1998: The formation of tropical cyclones. *Meteor. Atmos. Phys.,* **67,** 37–69, doi:10.1007/BF01277501.

Hodges, K. I., D. W. Chappel, G. J. Robinson, and G. Yang, 2000: An improved algorithm for generating global window brightness temperatures from multiple satellite infrared imagery. *J. Atmos. Oceanic Technol.,* **17,** 1296–1312, doi:10.1175/1520-0426(2000)017<1296:AIAFGG>2.0.CO;2.

Hopsch, S. B., C. D. Thorncroft, K. Hodges, and A. Aiyyer, 2007: West African storm tracks and their relationship to Atlantic tropical cyclones. *J. Climate,* **20,** 2468–2483, doi:10.1175/JCLI4139.1.

——, ——, and K. R. Tyle, 2010: Analysis of African easterly wave structures and their role in influencing tropical cyclogenesis. *Mon. Wea. Rev.,* **138,** 1399–1419, doi:10.1175/2009MWR2760.1.

Houze, R. A., Jr., 2004: Mesoscale convective systems. *Rev. Geophys.,* **42,** RG4003, doi:10.1029/2004RG000150.

Jenkins, G. S., and A. Pratt, 2008: Saharan dust, lightning and tropical cyclones in the eastern tropical Atlantic during NAMMA-06. *Geophys. Res. Lett.,* **35,** L12804, doi:10.1029/2008GL033979.

——, ——, and A. Heymsfield, 2008: Possible linkages between Saharan dust and tropical cyclone rain band invigoration in the eastern Atlantic during NAMMA-06. *Geophys. Res. Lett.,* **35,** L08815, doi:10.1029/2008GL034072.

——, and Coauthors, 2010: Coastal observations of weather features in Senegal during the African Monsoon Multidisciplinary Analysis special observing period 3. *J. Geophys. Res.,* **115,** D18108, doi:10.1029/2009JD013022.

Karyampudi, V. M., and T. N. Carlson, 1988: Analysis and numerical simulations of the Saharan air layer and its effect on easterly wave disturbances. *J. Atmos. Sci.,* **45,** 3102–3136, doi:10.1175/1520-0469(1988)045<3102:AANSOT>2.0.CO;2.

——, and H. F. Pierce, 2002: Synoptic-scale influence of the Saharan air layer on tropical cyclogenesis over the eastern Atlantic. *Mon. Wea. Rev.,* **130,** 3100–3128, doi:10.1175/1520-0493(2002)130<3100:SSIOTS>2.0.CO;2.

Kiladis, G. N., C. D. Thorncroft, and N. M. J. Hall, 2006: Three-dimensional structure and dynamics of African easterly waves. Part I: Observations. *J. Atmos. Sci.,* **63,** 2212–2230, doi:10.1175/JAS3741.1.

Leduc-Leballeur, M., G. de Coëtlogon, and L. Eymard, 2013: Air–sea interaction in the Gulf of Guinea at intraseasonal timescales: Wind bursts and coastal precipitation in boreal spring. *Quart. J. Roy. Meteor. Soc.,* **139,** 387–400, doi:10.1002/qj.1981.

Leppert, K. D., D. J. Cecil, and W. A. Petersen, 2013: Relation between tropical easterly waves, convection, and tropical cyclogenesis: A Lagrangian perspective. *Mon. Wea. Rev.,* **141,** 2649–2668, doi:10.1175/MWR-D-12-00217.1.

Maddox, R. A., 1980: Mesoscale convective complexes. *Bull. Amer. Meteor. Soc.,* **61,** 1374–1387, doi:10.1175/1520-0477(1980)061<1374:MCC>2.0.CO;2.

Mapes, B. E., and R. A. Houze, 1993: Cloud clusters and superclusters over the oceanic warm pool. *Mon. Wea. Rev.,* **121,** 1398–1416, doi:10.1175/1520-0493(1993)121<1398:CCASOT>2.0.CO;2.

Mathon, V., and H. Laurent, 2001: Life cycle of Sahelian mesoscale convective cloud systems. *Quart. J. Roy. Meteor. Soc.,* **127,** 377–406, doi:10.1002/qj.49712757208.

McBride, J. L., and R. Zehr, 1981: Observational analysis of tropical cyclone formation, Part II: Comparison of non-developing versus developing systems. *J. Atmos. Sci.,* **38,** 1132–1151, doi:10.1175/1520-0469(1981)038<1132:OAOTCF>2.0.CO;2.

Menard, R. D., and J. M. Fritsch, 1989: A mesoscale convective complex-generate inertially stable warm core vortex. *Mon. Wea. Rev.,* **117,** 1237–1261, doi:10.1175/1520-0493(1989)117<1237:AMCCGI>2.0.CO;2.

Meynadier R., O. Bock, S. Gervois, F. Guichard, J.-L. Redelsperger, A. Agusti-Panareda, and A. Beljaars, 2010: West African monsoon water cycle: 2. Assessment of numerical weather prediction water budgets. *J. Geophys. Res.,* **115,** D19107, doi:10.1029/2010JD013919.

Nzeukou, A., and H. Sauvageot, 2002: Distribution of rainfall parameters near the coasts of France and Senegal. *J. Appl. Meteor.,* **41,** 69–82, doi:10.1175/1520-0450(2002)041<0069:DORPNT>2.0.CO;2.

Pasch, R. J., L. A. Avila, and J. G. Jiing, 1998: Atlantic tropical systems of 1994 and 1995: A comparison of a quiet season to a near-record-breaking one. *Mon. Wea. Rev.,* **126,** 1106–1123, doi:10.1175/1520-0493(1998)126<1106:ATSOAA>2.0.CO;2.

Peng, M. S., B. Fu, T. Li, and D. E. Stevens, 2012: Developing versus nondeveloping disturbances for tropical cyclone

formation. Part I: North Atlantic. *Mon. Wea. Rev.,* **140,** 1047–1066, doi:10.1175/2011MWR3617.1.

Pytharoulis, I., and C. D. Thorncroft, 1999: The low-level structure of African easterly waves in 1995. *Mon. Wea. Rev.,* **127,** 2266–2280, doi:10.1175/1520-0493(1999)127<2266:TLLSOA>2.0.CO;2.

Raymond, D. J., and H. Jiang, 1990: A theory for long-lived convective systems. *J. Atmos. Sci.,* **47,** 3067–3077, doi:10.1175/1520-0469(1990)047<3067:ATFLLM>2.0.CO;2.

Reed, R., D. Norquist, and E. Recker, 1977: The structure and properties of African wave disturbances as observed during phase III of GATE. *Mon. Wea. Rev.,* **105,** 317–333, doi:10.1175/1520-0493(1977)105<0317:TSAPOA>2.0.CO;2.

Ritchie, E. A., and G. J. Holland, 1997: Scale interactions during the formation of Typhoon Irving. *Mon. Wea. Rev.,* **125,** 1377–1396, doi:10.1175/1520-0493(1997)125<1377:SIDTFO>2.0.CO;2.

——, J. Simpson, W. T. Liu, J. Halverson, C. Velden, K. F. Brueske, and H. Pierce, 2003: Present day satellite technology for hurricane research: A closer look at formation and intensification. *Hurricane! Coping with Disaster,* R. Simpson, Ed., Amer. Geophys. Union, 249–289.

Saha, S., and Coauthors, 2010: The NCEP Climate Forecast System Reanalysis. *Bull. Amer. Meteor. Soc.,* **91,** 1015–1057, doi:10.1175/2010BAMS3001.1.

Sall, S. M., and H. Sauvageot, 2005: Cyclogenesis off the African coast: The case of Cindy in August 1999. *Mon. Wea. Rev.,* **133,** 2803–2813, doi:10.1175/MWR3003.1.

——, ——, A. Gaye, A. Viltard, and P. de Felice, 2006: A cyclogenesis index for tropical Atlantic off the African coasts. *Atmos. Res.,* **79,** 123–147, doi:10.1016/j.atmosres.2005.05.004.

Shapiro, L. J., and S. B. Goldenberg, 1998: Atlantic sea surface temperatures and tropical cyclone formation. *J. Climate,* **11,** 578–590, doi:10.1175/1520-0442(1998)011<0578:ASSTAT>2.0.CO;2.

Simpson, J., E. Ritchie, G. J. Holland, J. Halverson, and S. Stewart, 1997: Mesoscale interactions in tropical cyclone genesis. *Mon. Wea. Rev.,* **125,** 2643–2661, doi:10.1175/1520-0493(1997)125<2643:MIITCG>2.0.CO;2.

Sippel, J. A., S. A. Braun, and C.-L. Shie, 2011: Environmental influences on the strength of Tropical Storm Debby (2006). *J. Atmos. Sci.,* **68,** 2557–2581, doi:10.1175/2011JAS3648.1.

Small, R. J., and Coauthors, 2008: Air–sea interaction over ocean fronts and eddies. *Dyn. Atmos. Oceans,* **45,** 274–319, doi:10.1016/j.dynatmoce.2008.01.001.

Thorncroft, C., and K. Hodges, 2001: African easterly wave variability and its relationship to Atlantic tropical cyclone activity. *J. Climate,* **14,** 1166–1179, doi:10.1175/1520-0442(2001)014<1166:AEWVAI>2.0.CO;2.

——, J. Lafore, G. Berry, R. Roca, F. Guichard, M. Tomasini, and N. Asencio, 2007: Overview of African weather systems during the summer 2006. *CLIVAR Exchanges,* No. 12, International CLIVAR Project Office, Southampton, United Kingdom, 18–20.

——, H. Nguyen, C. Zhang, and P. Peyrille, 2011: Annual cycle of the West African monsoon: Regional circulations and associated water vapour transport. *Quart. J. Roy. Meteor. Soc.,* **137,** 129–147, doi:10.1002/qj.728.

Vizy, E. K., and K. H. Cook, 2009: Tropical storm development from African easterly waves in the eastern Atlantic: A comparison of two successive waves using a regional model as part of NASA AMMA 2006. *J. Atmos. Sci.,* **66,** 3313–3334, doi:10.1175/2009JAS3064.1.

Zehr, R., 1992: Tropical cyclogenesis in the western North Pacific. NOAA Tech. Rep. NESDIS 16, 181 pp.

Zipser, E. J., and Coauthors, 2009: The Saharan air layer and the fate of African easterly waves—NASA's AMMA field study of tropical cyclogenesis. *Bull. Amer. Meteor. Soc.,* **90,** 1137–1156, doi:10.1175/2009BAMS2728.1.